Tiny grains shining bright in the gaps of Herbig Ae transitional discs

Eloise K. Birchall [1]* Michael J. Ireland [1]* Christoph Federrath,[1] John D. Monnier,[2] Stefan Kraus,[3] Matthew Willson,[3] Adam L. Kraus,[4] Aaron Rizzuto,[4] Matthew T. Agnew[5] and Sarah T. Maddison[5]

[1]*Research School of Astronomy and Astrophysics, Australian National University, Canberra, 2611 ACT, Australia*
[2]*Department of Astronomy, University of Michigan, Ann Arbor, MI 48109, USA*
[3]*Astrophysics Group, School of Physics, University of Exeter, Stocker Road, Exeter EX4 4QL, UK*
[4]*Department of Astronomy, The University of Texas at Austin, Austin, TX 78712, USA*
[5]*Centre for Astrophysics and Supercomputing, Swinburne University of Technology, Hawthorn, VIC 3122, Australia*

ABSTRACT

This work presents a study of two Herbig Ae transitional discs, Oph IRS 48 and HD 169142; which both have reported rings in their dust density distributions. We use Keck-II/NIRC2 adaptive optics imaging observations in the L′ filter (3.8 μm) to probe the regions of these discs inwards of ~20 au from the star. We introduce our method for investigating these transitional discs, which takes a forward modelling approach: making a model of the disc (using the Monte Carlo radiative transfer code RADMC3D), convolving it with point spread functions of calibrator stars, and comparing the convolved models with the observational data. The disc surface density parameters are explored with a Monte Carlo Markov Chain technique. Our analysis recovers emission from both of the discs interior to the well-known optically thick walls, modelled as a ring of emission at ~15 au in Oph IRS 48, and ~7 au for HD 169142, and identifies asymmetries in both discs. Given the brightness of the near-symmetric rings compared to the reported companion candidates, we suggest that the reported companion candidates can be interpreted as slightly asymmetric disc emission or illumination.

Key words: protoplanetary discs – stars: individual: Oph IRS 48 and HD 169142 – radiative transfer.

1 INTRODUCTION

Transitional discs are a subset of protoplanetary discs that have a region which is depleted in dust (but not necessarily depleted in gas), known as a gap or hole. These objects are a subset of Lada (1987) Class II objects, with flat or declining mid-infrared (mid-IR) excesses in their spectral energy distributions (SEDs). Giant planets that have formed in protoplanetary discs are predicted to carve out gaps or holes, producing structures that might be observed in transitional discs (Strom et al. 1989; Skrutskie et al. 1990; Marsh & Mahoney 1992, 1993). It has also been suggested that the gaps in protoplanetary discs could be caused by multiplanet systems (Dodson-Robinson & Salyk 2011), however the prevalence of systems with three or more Jupiter mass planets is very low (<1 per cent, Han et al. 2014), so this is unlikely to be the only cause of transitional disc structure. By direct imaging of transitional discs, we can look for signs of planet formation or other disc evolution

such as dust asymmetries, dust depleted regions, gaps, rings, and holes.

The transitional discs studied in this work are Oph IRS 48 and HD 169142. Both are Herbig Ae stars known to have polycyclic aromatic hydrocarbons (PAHs) in their discs. Information on these objects is summarized in Table 1. Both objects are known to have structure in their outer discs with rings of emission at 50–60 au identified from observations at mm wavelengths (e.g. Geers et al. 2007a; Brown et al. 2012b; van der Marel et al. 2013; Quanz et al. 2013; Maaskant et al. 2014).

There are several objects for which there are detections of dust within the regions thought to be depleted of CO. This is the case for V1247 Orionis, for which the presence of carbon-rich dust inside the gap region has been found through near-IR observations (Kraus et al. 2013). Previous modelling of IR spectra of both Oph IRS 48 and HD 169142 have indicated the likely presence of PAHs within the gas gap regions (regions depleted in CO; Geers et al. 2007b; Maaskant et al. 2014; Seok & Li 2017).

Oph IRS 48 is located in the ρ Ophiuchus star forming region, as catalogued by Elias (1978) and confirmed by Wilking, Lada & Young (1989). The average distance to the cloud's core was

* E-mail: eloise.birchall@anu.edu.au (EKB); michael.ireland@anu.edu.au (MJI)

Table 1. Parameters of Oph IRS 48 and HD 169142.

Oph IRS 48		
Right ascension	16h 27m 37.190s	1
Declination	$-24°30'35.03''$	1
Alternate names	WLY 2-48,	1
	2MASS J16273718−2430350,	1
	YLW 46	1
Stellar type	A0	2, 3
Distance to object	134.4 ± 2.2 pc	4
W1 magnitude	5.786	5
HD 169142		
Right ascension	18h 24m 29.779s	1
Declination	$-29°46'49.37''$	1
Alternate names	MWC 925	1
Stellar type	A5	6
Distance to object	114.0 ± 0.8 pc	4
W1 magnitude	6.203	5

Notes: 1. SIMBAD: simbad.u-strasbg.fr/; 2. McClure et al. (2010); 3. Brown et al. (2012a); 4.Gaia Collaboration et al. (2018); 5. WISE All-Sky Catalog; and 6. Seok & Li (2016).

$120.0^{+4.5}_{-4.2}$ pc found by Loinard et al. (2008) using Very Long Baseline Array data. The parallax for Oph IRS 48 as given by *Gaia* DR2 (Gaia Collaboration et al. 2018) is 7.44 ± 0.12 millisecond of arc (mas), corresponding to a distance of $\sim 134.4 \pm 2.2$ pc, and this is the distance adopted in this work.

The outer disc of Oph IRS 48 is known to have a strong asymmetric feature in the millimetre-sized grains. The asymmetry in the dust of the outer disc (at a deprojected distance of 67 au from the star) was discovered with Atacama Large Millimetre/submillimetre Array (ALMA) sub-millimetre observations and indicates a separation of the micro- and millimetre-sized dust grains (van der Marel et al. 2013). There is also a separation of the very small grains that do not follow the larger micron sized dust, as reported as unresolved emission in Geers et al. (2007a). Later observations found that centimetre-sized dust grains are further concentrated in the region of the millimetre grains (van der Marel et al. 2015), consistent with being caused by a vortex induced by a pressure or density gradient generating a dust trap, which may have been generated by a companion (van der Marel et al. 2013, 2015).

Inside the 67 au asymmetric ring, the structure of the Oph IRS 48 disc becomes more complicated. It is thought that there is a depletion of dust within 67 au, given that there is a no excess at wavelengths short of $10\,\mu$m in the SED (Maaskant et al. 2013). However, where these depletions are seen can depend on the wavelength of the observations, as different materials (gas, dust, PAHs, large or small grains) are traced by different wavelengths (e.g. Brown et al. 2012b). The disc is considered to be mostly depleted of dust within ~ 23 au (Bruderer et al. 2014), where there is a wall, but the flux deficit caused by depletion depends strongly on the wavelength of observation. Oph IRS 48 is still accreting (accretion rate $\sim 10^{-9}\,M_\odot\,yr^{-1}$, Salyk et al. 2013), and SED modelling also confirms the presence of inner disc material (e.g. Bruderer et al. 2014).

HD 169142 was previously thought from optical photometry to be located at a distance of 145 pc (Sylvester et al. 1996), but the parallax was measured with *Gaia* (Gaia Collaboration et al. 2018) to be 8.77 ± 0.06 mas, corresponding to a distance of 114.0 ± 0.8 pc. We adopt the new distance in this work, and have adjusted the linear radii of the previously noted features to correspond to the new distance.

HD 169142 was reported as having circumstellar material by Walker & Wolstencroft (1988), and subsequent studies have found that this disc has structure, including an inner cavity and rings (e.g. Panić et al. 2008; Honda et al. 2012; Quanz et al. 2013; Osorio et al. 2014; Seok & Li 2016; Monnier et al. 2017; Fedele et al. 2017; Macías et al. 2017). The most commonly modelled structure for HD 169142 thus far includes a small inner rim (Panić et al. 2008; Honda et al. 2012), with an optically thick ring at ~ 20 au (Osorio et al. 2014; Honda et al. 2012; Panić et al. 2008; Bertrang et al. 2018), and a gap from 31 au to an optically thick wall at 55 au (Quanz et al. 2013; Bertrang et al. 2018).

It is possible that the gaps in the disc are caused by planet–disc interactions. Biller et al. (2014) and Reggiani et al. (2014) suggested from L′ ($3.8\,\mu$m) observations using a coronagraph that a potential companion is located at a distance of either ~ 13 au (110 ± 30 mas, position angle of $0 \pm 14°$, Biller et al. 2014) or ~ 18 au (156 ± 32 mas, position angle of $7.4 \pm 11.3°$, Reggiani et al. 2014) from the star (interior to the ~ 20 au ring). The potential companion has an L′ apparent Vega magnitude of 12.2 ± 0.5 mag (Reggiani et al. 2014), which corresponds to a contrast of 6.4 mag (Biller et al. 2014), or 6.5 ± 0.5 mag (Reggiani et al. 2014). These studies both used observations taken with the Very Large Telescope using the Nasmyth Adaptive Optics System Near-IR Imager and Spectrograph (NACO), and the coronograph available for this instrument. Both studies used similar methods to detect the candidate companion, which included angular differential imaging (ADI) that self-subtracted any azimuthally symmetric structures. Other studies investigate whether this possible companion, and potentially a second candidate companion further out in the disc are causing the structural features seen in the disc (Fedele et al. 2017; Kanagawa et al. 2015).

There have been few previous imaging studies of these discs at wavelengths shorter than $\sim 8\,\mu$m – wavelengths most sensitive to structures inside the known rings and where planet formation signatures, including those of circumplanetary accretion discs (Zhu 2015), could be seen. The key reason for this gap is the higher contrasts and angular resolutions needed for shorter wavelengths, meaning that specialized techniques are required, such as ADI (Reggiani et al. 2014), or aperture mask interferometry (Schworer et al. 2017).

It is possible that there is a companion in each of the discs, clearing the gaps, and driving the asymmetries (e.g. van der Marel et al. 2013; Biller et al. 2014; Reggiani et al. 2014). To investigate whether there is a planet inside the gas gaps of these discs at ~ 20 au, we present our observations and analysis of both discs as follows. Section 2 discusses the observations used for this work, which differs from previous studies as we are more sensitive to extended structures than aperture mask interferometry, but are still sensitive to circularly symmetric features, unlike ADI. Section 3 discusses evidence for significant emission inside the previously inferred walls. Sections 4 and 5 outline the computational methods used in this paper and tests them on a synthetic data set. Section 6 describes the resulting best-fitting physical disc models. Section 7 summarizes our results in the context of the field, and discusses possible future work in this area.

2 OBSERVATIONS AND DATA REDUCTION

2.1 Observations

Observations were acquired with the NIRC2 instrument on Keck II over three observing runs (June 2014–2016). All observations

Table 2. Observations.

Target	Date	T int (s)	Co-adds	Exposure time (s)	Frames	Visits	Seeing (arcmin)	Airmass	Calibrators (visits)
HD 169142	2014 June 10	0.053	200	10.6	8, 4	2	0.70	1.61	HD 167666 (1), HD 170768 (2)
Oph IRS 48	2015 June 23	0.1	100	10	18	1	0.30	1.40	Elia 2-24 (1), Elia 2-26 (1), WSB 52 (1)
Oph IRS 48	2016 June 16	0.2	100	20	8, 10	2	No data	1.52, 1.42	GSS 37 (2), DoAr 32 (2), DoAr 24 (2), WSB 12 (2), DoAr 33 (2), WSB 52 (1), WSB 52/[WMR2005] 2-30 (1), [MMG98] RX J1622.9-2326 (2)
HD 169142	2016 June 17	0.2	100	20	10	1	0.95	1.56	HD 167666 (1)

Notes: All of these observations were taken in the L′ filter using the NIRC2 instrument on the Keck II telescope.
Column 1: target name. Column 2: date the observations were taken. Column 3: integration time for each co-add in seconds. Column 4: number of co-adds (snapshots that make up the final image). Column 5: total exposure time in seconds, integration time multiplied by co-adds. Column 6: frames taken each visit. Column 7: number of visits to that target that night. Column 8: the seeing is taken as the mean seeing for that night from the Canada–France–Hawaii Telescope seeing monitor and is in the V filter. Column 9: airmass the target was observed through. Column 10: calibrators used (number of visits to calibrator).

used in this work were taken with the L′ filter of the NIRC2 camera, using a 'large hex pupil', a 512 × 512 subarray, and a two-point dither mode separated by ∼3.5 arcsec, utilizing the top left and bottom right quadrants of the detector. These observations did not use aperture masking or coronography. Table 2 summarizes these observations, including total exposure times and point spread function (PSF) calibrators. We use both natural and laser guide star adaptive optics (AO) in this work (because HD 169142 is bright enough to not need the laser, and Oph IRS 48 is fainter). Our 2014 and 2016 observations of HD 169142 used natural guide star AO and the 2015 and 2016 observations of Oph IRS 48 used laser guide star AO.

The calibrators for HD 169142 were chosen specifically for that object, while Oph IRS 48 was calibrated against other Class II objects that formed a survey of the Ophiuchus star-forming region for accreting exoplanets. These calibrators were expected to have bright, unresolved inner discs, with cross-calibration between different calibrators used to check for any measurably resolved objects. No potential calibrators were eliminated.

2.2 Data reduction

Each image was corrected for detector non-linearity using the algorithm from the IDL program `linearize_nirc2.pro`,[1] and then divided by a mean dome flat-field. Images taken with the star at the opposite dither position were used as an estimate of sky, which was subtracted from each image. Bad pixels were primarily identified by searching for outliers in mean pixel value or variance in a sequence of dark or flat frames. Additional bad pixels or cosmic rays were found by Fourier transforming each data frame, masking out spatial frequencies below Nyquist, inverse transforming and searching for significant peaks. The bad pixels were corrected using the algorithm in Ireland (2013), which involves finding the pixel value that minimizes Fourier power above the Nyquist frequency. Images were also centred to the peak value (which is typically the centre of the star) and cropped to 128 × 128 pixels, to remove edge effects.

When making the set of cleaned images to be used for subsequent analysis, images extincted by cloud by more than a factor of 2 or with

Strehl more than ∼20 per cent below the maximum were rejected. For the 2014 HD 169142 data, only one of the 12 target images was rejected. For the 2015 Oph IRS 48 data, three of the 18 target images were rejected. For the 2016 HD 169142 data, two of the 10 target images were rejected. For the 2016 Oph IRS 48 data, six of the 18 target images were rejected. The 2016 data were taken through cloud, and for all data sets we began data acquisition before the low-bandwidth wavefront sensor showed low errors. All raw data are publicly available in the Keck observatory archive, and we have made the cleaned data cubes[2] available.

3 RESOLVED DISC EMISSION
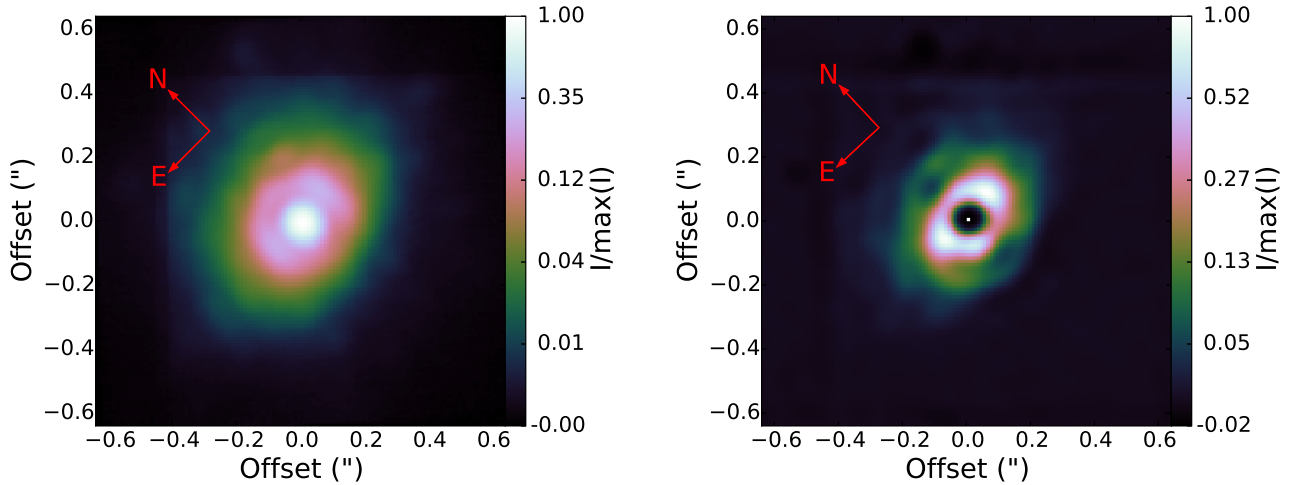
3.1 Richardson–Lucy deconvolution

The Richardson–Lucy method of deconvolution is an iterative deconvolution method based on finding the mostly likely image that fits a data set given a known PSF. It was developed independently by Richardson (1972) and Lucy (1974). We performed a Richardson–Lucy deconvolution on our reduced data, in order to isolate the resolved structure in the discs, and as a simple first-pass imaging algorithm to inspire physical model-fitting.

We used 50 iterations of the Richardson–Lucy algorithm, and our initial model was a point source. We used this algorithm on all target–calibrator-image pairs. However, we only considered the calibrator image that, when convolved, had the smallest root mean square (rms) with respect to the target star image (i.e. the one that returned the image most similar to each target image). We chose to use 50 iterations because at this point the rms between the target and calibrator images is stable, and not decreasing dramatically with more iterations. Also, with more iterations, the deconvolution noticeably over fits the data.

One should note that the point-source initial model for our implementation of the Richardson–Lucy algorithm has an effect of regularizing the final model to be a point source with resolved structure, rather than a marginally resolved central source with structure. A point source with a disc is a suitable physical approximation for our deconvolved images as the star and its inner ring of material (< 1 au) is unresolved.

---

[1]http://www.astro.sunysb.edu/metchev/ao.html

[2]http://www.mso.anu.edu.au/∼mireland/Birchall18/

Figure 1. Left: reduced data for Oph IRS 48. Right: deconvolved, point source subtracted image of Oph IRS 48. The central bright point shows where the star would be. Arrows show the direction of north and east. Images have arcsinh colour scaling, and are normalized to the maximum intensity of the image.
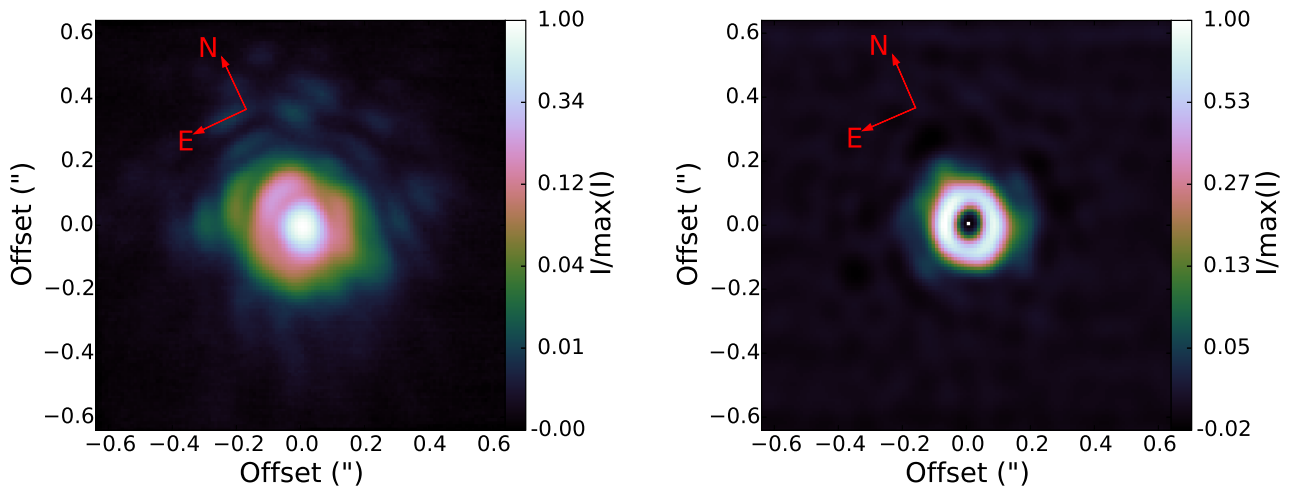
Figure 2. Left: reduced data for HD 169142. Right: deconvolved, point source subtracted image of HD 169142. The central bright point shows where the star would be. Arrows show the direction of north and east. Images have arcsinh colour scaling, and are normalized to the maximum intensity of the image.

The deconvolved images for Oph IRS 48 and HD 169142 are shown in the right-hand panels of Figs 1 and 2. In both cases, a resolved ring of emission is clearly visible at radii within the previously published transitional disc holes ($\sim$23 au for Oph IRS 48, and $\sim$20 au for HD 169142).

3.2 Fourier analysis

The presence of significant rings interior to the $\sim$20 au wall inferred from previous data sets (e.g. Bruderer et al. 2014; Osorio et al. 2014, for Oph IRS 48 and HD 169142, respectively) in the Richardson–Lucy deconvolved images is something that could in principle also arise from instability in the AO system. This possibility was ameliorated in our data collection by having multiple epochs on the targets and multiple calibrators at each epoch. In addition, Strehl ratios were reasonably high (0.5–0.7) and stable (within $\sim$10 per cent in the used images) given the long wavelength of our observation.

In order to quantitatively examine the effects of different calibrators, we performed a power spectrum analysis, as pioneered in speckle interferometry (Labeyrie 1970), where spatial power spectra were calculated for both individual calibrator stars and target stars, and then divided by the mean of the PSF calibrator power spectra in two dimensions. These calibrated power spectra are then equal to the power spectrum of the target itself, with the dispersion amongst the calibrator power spectra representing the uncertainty in this technique.

We plot the azimuthal averages of the visibilities (i.e. the square root of the power spectra) from each non-rejected frame of the target and calibrator in Figs 3 and 4 for the 2014 and 2015 epochs, divided by the mean azimuthally averaged visibilities. It can be seen that for both HD 169142 and Oph IRS 48, the target visibility curves fall well outside the range of the calibrators, indicative of dominant structures that are fully resolved on 0.2–0.3 arcsec scales. The asymptotic visibilities of $\sim$0.26 for Oph IRS 48 and $\sim$0.57 for HD 169142 measures directly that only $\sim$26 per cent and $\sim$57 per cent of the L' flux from Oph IRS 48 and HD 169142 come from the sum of the central star and inner disc, in disagreement with previous models constrained by the SED (e.g. Seok & Li 2016; Bruderer et al. 2014, for HD 169142 and Oph IRS 48, respectively).
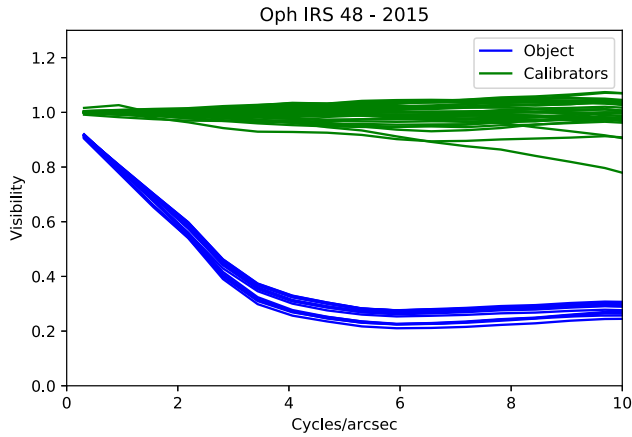
Figure 3. The azimuthally averaged power spectrum for Oph IRS 48 and calibrators for the 2015 epoch. Each line represents one saved 10 s exposure. In this domain, it is both very clear that the target is well resolved and that the calibrators have stable visibilities (square root of power) with a standard deviation of $\lesssim 5$ per cent.
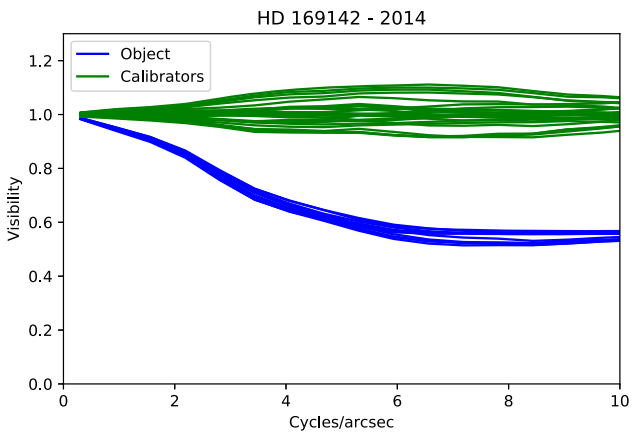

Figure 4. The same as Fig. 3, for HD 169142 (for the 2014 epoch).

In order to further analyse these visibilities, we used a model where each target was represented by an azimuthally symmetric inclined thin disc. The deprojected spatial frequency coordinate r'_{uv} is derived from the (u, v) coordinate using:

$$r'_{uv} = \sqrt{r^2_{uv} \cos(\theta_{uv} - \theta_{maj})^2 + r^2_{uv} \sin(\theta_{uv} - \theta_{maj})^2 \cos(i)}, \quad (1)$$

where θ_{uv} is the position angle of the (u, v) coordinate, r_{uv} its magnitude, θ_{maj} the position angle of the disc major axis, and i the disc inclination. The Fourier power was then binned and averaged over this deprojected Fourier coordinate r'_{uv} to enable robust data visualization and azimuthally symmetric fitting. For Oph IRS 48, an inclination of $55°$ and a major axis position angle of $99°$ were used, while for HD 169142, an inclination of $30°$ and position angle of $13°$ were used (based on literature values and our findings in Section 6 – where they differ from literature values). After azimuthally averaging the deprojected power spectra and taking the square root, we plot the visibility curves in Fig. 5. Rising visibilities to mid or high spatial frequencies demonstrate that fits of ring-like or sharp-edged flux distributions are appropriate, rather than e.g. Gaussian or power-law dust distributions. We fitted several parametrized models to these distributions in order to determine the required model complexity (Table 3 and Fig. 5). One ring at
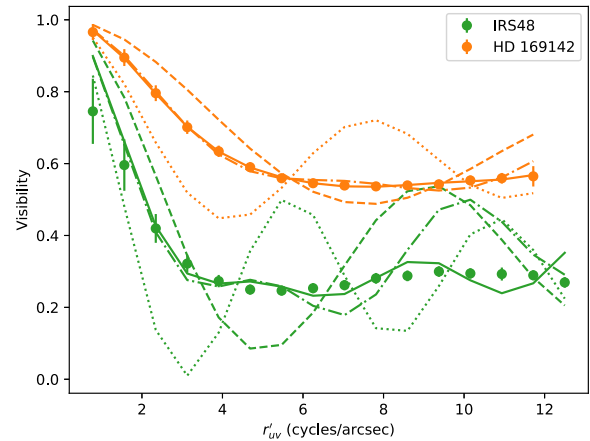
Figure 5. Deprojected, azimuthally averaged visibility curves for Oph IRS 48 (green) and HD 169142 (orange). The circles represent the visibility measurements. Various models are fitted to these data: single rings at the previous literature location of walls (dotted lines); single rings at variable locations (dashed lines); two rings at variable locations (dotted–dashed lines); and three rings at variable locations (solid lines). For both objects, one ring is a poor fit to this azimuthally averaged data, and at least two rings or a disc with this many free parameters, is required.

Table 3. Tested radii and fluxes for rings in Oph IRS 48 and HD 169142, where F refers to the fraction of flux that comes from each ring of radius r. The visibility curves generated by these model systems are shown in Fig. 5.

		Oph IRS 48			
F_1	r_1 (au)	F_2	r_2 (au)	F_3	r_3 (au)
0.71	–	–	–	–	–
0.66	14.3	–	–	–	–
0.38	12.7	0.29	25.2	–	–
0.22	9.8	0.26	17.0	0.20	26.9
		HD 169142			
F_1	r_1 (au)	F_2	r_2 (au)	F_3	r_3 (au)
0.40	–	–	–	–	–
0.37	11.0	–	–	–	–
0.26	10.7	0.14	20.7	–	–
0.24	10.2	0.12	18.6	0.03	28.4

the previous location of the wall inferred from the SED or long-wavelength observations is clearly inconsistent with the data, which requires a more continuous distribution of emission, including an emission component inside the previous ($\sim$20 au) gap.

4 THEORETICAL DISC MODELLING

In order to interpret the observational data, radiative transfer models of the discs were generated. We chose to follow previous literature on these discs, (e.g. Bruderer et al. 2014, Oph IRS 48) and to fit power-law surface density distributions with multiple gaps. We recognize that alternative models with smoother distributions of dust and gas may fit our data equally well, and could be attempted as an extension to this work, constrained by hydrodynamical models or more detailed SED modelling, for example. Limitations of our work are discussed in Section 4.2.5. The radiative transfer disc models used in this work are made using RADMC3D (Dullemond

2012),[3] which is a Monte Carlo radiative transfer code. A forward modelling approach was taken; the models are generated by this code, rotated to match the observed position angle at each epoch, and convolved with a PSF so that a comparison can be made between the model and the observational data.

The radiative transfer models are discussed in Section 4.1, and the details of the parameters of the models are in Section 4.2.

4.1 Radiative transfer

The protoplanetary disc function of RADMC3DPY, the companion PYTHON library to RADMC3D (Dullemond 2012), was used to create 3D disc density distributions with structures such as gaps and rings, which were then fed into RADMC3D.

Three model types are tested; a symmetric disc, an asymmetric disc and an asymmetric disc with a companion, with each model type being an extension on the previous one. These three model types are used to identify the presence of asymmetries in the data and attempt to characterize the asymmetry to see if it is point-like. To simulate an asymmetric disc, the central star can be moved slightly which gives an asymmetric dust illumination. In some cases, companions can cause the disc to become eccentric (Thalmann et al. 2010), meaning that the star is no longer at the centre of the disc. Sub-stellar companions are simulated by adding photospheric emission from a second point source to the RADMC3D disc model. The companion source is less massive, smaller in radius and cooler than the central star. The parameters involved in generating these models are discussed in Section 4.2.

4.2 Parameters

4.2.1 Globally constant parameters

The stellar emission type, dust model, and stellar source type were held constant for both objects. We use Kurucz[4] (Castelli & Kurucz 2004) stellar models, with solar abundances and microturbulence of $2 \, \mathrm{km \, s^{-1}}$ (an arbitrary choice, as we are not attempting to model the spectrum of the star in detail). The RADMC3D emission source used for either object is a point source.

The chosen dust model used for the final modelling of both objects is a fine-grained carbon and PAH dust mixture (henceforth CP dust). The dust model chosen was the Draine & Li (2001, 2007) dust, which includes carbon in graphitic form and also grain sizes down to nm scale which are mostly PAHs. The discs of both Oph IRS 48 and HD 169142 are known to contain PAHs (e.g. Geers et al. 2007b; Maaskant et al. 2014; Seok & Li 2016, Oph IRS 48, both, HD 169142, respectively). The reasoning behind the choice of dust is explained further in Section 6.1. The dust best suited from the Draine & Li (2001, 2007) set of neutral dust was a grain size of $5.6 \times 10^{-3} \, \mathrm{\mu m}$ (5.6 nm). At 5.6 nm, the dust mixture can give strong PAH features, but also has a contribution from a more general graphitic source (Draine & Li 2001, 2007; Draine 2003). This 5.6 nm CP dust is used for the determination of the other disc parameters.

Other parameters that are the same for both objects include the number of photons (set to 10^6), and the spatial resolution. These were both set based on results of convergence tests, ensuring a

---

[3]Code is available at: http://www.ita.uni-heidelberg.de/~dullemond/softwa re/radmc-3d/
[4]http://kurucz.harvard.edu/grids.html

Table 4. Fixed parameters for Oph IRS 48 and HD 169142.

Set parameter	Oph IRS 48 Value	Reference
Stellar type	A0	1, 2
Star temperature	9000 K	2
Star mass	$2.0 \, \mathrm{M_\odot}$	2
Star radius	$2.24 \, \mathrm{R_\odot}$	Assumed (young A0 star)
Disc mass	$10^{-4} \, \mathrm{M_\odot}$	3
r_{wall}	67 au	4, adjusted to new distance
δ_{wall}	0.1	3
Dust type	5.6 nm C and PAH	Assumed, 5
Distance to object	134.4 pc	6
Flux ratio	7.8	This work

Set parameter	HD 169142 Value	Reference
Stellar type	A5	7
Star temperature	8250 K	7
Star mass	$1.65 \, \mathrm{M_\odot}$	7
Star radius	$1.56 \, \mathrm{R_\odot}$	Assumed, 7
Disc mass	$10^{-3} \, \mathrm{M_\odot}$	Assumed, 7
r_{wall}	55 au	8, 9
δ_{wall}	0.1	Assumed
Dust type	5.6 nm C and PAH	Assumed, 5
Distance to object	114 pc	6
Flux ratio	5.2	This work

Notes: 1. McClure et al. (2010); 2. Brown et al. (2012a); 3. Bruderer et al. (2014); 4. van der Marel et al. (2013); 5. Maaskant et al. (2014); 6. Gaia Collaboration et al. (2018); 7. Seok & Li (2016); 8. Quanz et al. (2013); and 9. Osorio et al. (2014).

reproducible output. The interested reader is directed to Appendix C for information on some of the other RADMC3D parameters that were used and convergence studies.

4.2.2 Object constant parameters

The stellar temperature and mass are fixed for each object based on literature spectral type and age for each object, with the radius coarsely adjusted to match the observed visible flux (Table 4). As we model the small-grained dust only, we cannot fit directly to the gas density. We choose to fix the mass of the disc (most of the mass is in the outer disc), to a value from the literature. Instead of a varying disc mass, we have a dust-to-gas mass ratio that is independent of radius, with density (of dust and gas) that is able to deviate from dust-to-gas ratio at various radii, as discussed in the next section. Both of the objects studied in this work are known to have either outer rings or asymmetries observed in much longer wavelengths (e.g. mm wavelengths), so we include these known parameters as the outer wall of the disc, r_{wall} and outer disc dust depletion δ_{wall}. The flux ratio refers to the ratio of flux between the star and the disc, and is discussed in more detail in Sections 4.2.4 and 6.1.

4.2.3 Parameters varied for each object

The symmetric model uses the following eight parameters: the overall dust-to-gas ratio; the inner radius of the disc r_{d}; the depletion factor of the inner disc, δ_{d}; the radius of the first wall, r_1; the depletion of the first gap, δ_1; the radius of the second wall, r_2; the inclination of the disc; and the position angle of the object on the
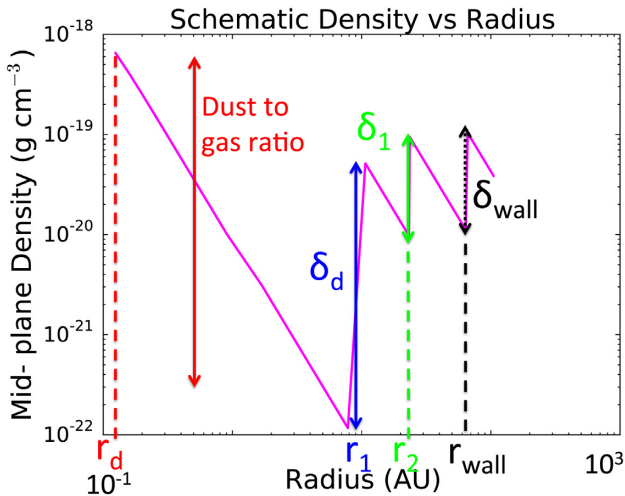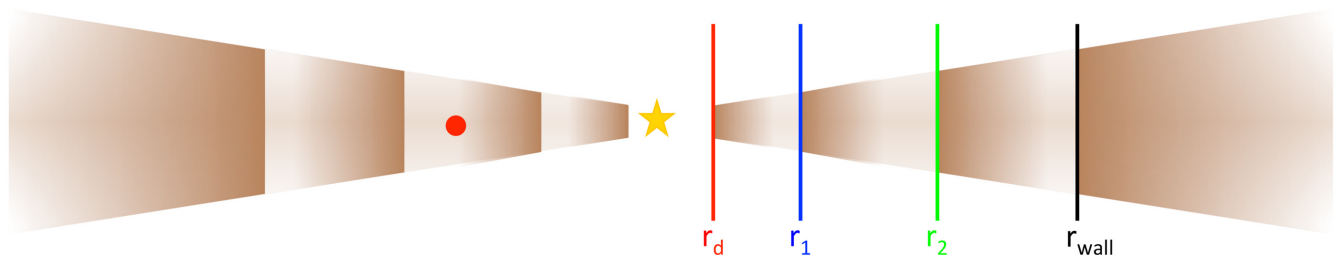
Figure 6. Shown here in magenta is a plot of the typical mid-plane density structure as a function of radius in the disc model. The parameters relating to the radii and density are marked. The dust-to-gas ratio, represented by the red arrow, moves the whole profile (magenta line) up or down. The first depletion factor, δ_d is that of the inner disc, and is marked with a blue arrow. It determines how depleted the inner disc is of material. The inner disc extends from r_d, marked in red, to r_1, marked in blue. The green arrow represents the depletion factor δ_1 between the two walls, r_1 (blue) and r_2 (green) that are allowed to vary in radius. The black arrow shows the set depletion factor, δ_{wall} for between these inner regions and the rest of the disc, at a distance of r_{wall} (black).

sky. The first six parameters are illustrated in a schematic plot of the mid-plane density of a disc in Fig. 6, and a schematic indicating the radii and other parameters is shown in Fig. 7. The inclination is whether the object is seen face-on, edge-on or somewhere in-between. The position angle quoted is the position angle of the disc major axis from north towards east, with the near side of the modelled disc at this position angle plus 90°. Note, however, that it is uncertain which minor axis corresponds to the near side.

The use of two walls in the disc at r_1 and r_2 allows us to explore the position of the known wall at r_2, while introducing a new wall at a closer radius, r_1. Both the objects investigated here are known to have rings of emission at a radius of ∼20 au, and so to recover the position of that ring, while also fitting our data we use two radii here.

The asymmetric model case moves the central star. Moving the central star simulates the appearance of an asymmetric disc, without making an asymmetric dust distribution, which could add

an arbitrary degree of complexity. For young stellar objects, it is possible for the star to be slightly offset from the centre of the disc, for example this was one explanation for the pericentre offset of LkCa15 (in e.g. Thalmann et al. 2010). The eccentricity of the disc in systems where the star has a pericentre offset is expected to be driven by the presence of a companion. The off-centre star placement means that one side of the disc is more strongly illuminated than the other, and is indicated by the position of the star in Fig. 7. The asymmetry parameters come from changing the *x* and *y* positions of the central star (units of this movement are in au). The positive *x*-direction is to the right along the semi-major axis, and the positive *y* direction is to the right along the semi-minor axis. These parameters are converted to a separation in mas and position angle offset when presented in Section 6.

The companion model is constructed by adding a second point source to the asymmetric disc model. We do not explicitly suggest that a point-like asymmetry is likely to be an accreting exoplanet at our poor angular resolution, but include a point source for simplicity of parametric modelling. The parameters that are varied in the model for the companion to ensure a better fit are the radius and *x* and *y* positions of the companion (where the *x*- and *y*-directions are the same as for the asymmetry). As with the star parameters, the position of the companion is converted to a separation given in mas and a position angle, so that it is more easily compared to literature values for the position of potential companions. The radius of the planet was used as a proxy for the brightness within our simulation setup and it is converted to a contrast of the companion to the total model, given in magnitudes. Please see Appendix B for details on the companion parameters. An example of a companion is denoted by the red circle in Fig. 7.

4.2.4 Priors

For some of the parameters that will be explored, Bayesian priors were set. The priors for the radii make sure that they stay in the order of $r_d < r_1 < r_2 < r_{wall}$. As minimum inner disc radius, we set 0.1 au, however, this prior is not important in the determination of the likelihood peak.

When the star is placed off-centre, there is a prior on the displacement so that the displacement does not exceed a radius of 1 au from its central position, which we find does not affect the likelihood peak.

There is also a prior on the flux ratio of the star to the total flux (star + disc). The flux ratio prior is used so that without actually modelling the full SED (which would require multiple dust models), we can still constrain the amount of dust in the unresolved inner

Figure 7. This is a schematic of our disc model. The colours are the same as in Fig. 6 – the red line indicates the inner edge of the disc, at the dust sublimation radius (r_d), and the black line is the radius of the wall known from mm-wavelength observations (r_{wall}). The blue line marks the radius of our new wall (r_1), and the green line marks the radius of the wall that is fitted based on mid-IR observations (r_2). The gradient in the brown colour indicates the density structure, which is illustrated in Fig. 6. The star is off-centre, to demonstrate how the asymmetry is introduced into the simulation, and the red circle indicates a companion, which can be placed anywhere in the mid-plane of the disc.

disc, and to have a self-consistent disc model that fully takes into account shadowing of the outer disc by the inner disc.

For both Oph IRS 48 and HD 169142, we fit the flux ratio of the entire disc and star system to the star. We calculate the flux ratio to fit by taking the stellar photosphere models of the objects from our simulations and literature observations at 3.4 (*Wide-field Infrared Survey Explorer*) or 3.6μm (*Spitzer*/IR Array Camera) photometry. To find our model flux ratio, we calculate the total intensity of a model with just a star, and for a model of a star and a disc, and then calculate the ratio of these intensities.

For Oph IRS 48 the flux ratio used was ∼7.8 and for HD 169142 it was ∼5.2. Uncertainties for each of the flux ratios are estimated for use in the EMCEE part of the method. The flux ratio places a constraint on the brightness of the disc in the model, and in particular, the unresolved inner disc.

4.2.5 Limitations

There are some limitations to our method and the way our models are constructed. Our models have a similar power-law density structure to those used in other works (e.g. Bruderer et al. 2014; Maaskant et al. 2014, Oph IRS 48, both, respectively), as seen in Fig. 6. Alternative density structures (e.g. without discontinuities) would also fit the data, however we choose to analyse one class of models with sufficient parameters. We consider a phenomenological model, and do not test whether the vertical structure is in equilibrium. We also assume that the distances to the objects are fixed, and do not use the uncertainties associated with them in our modelling. The interested reader is directed to Appendix C for more details on the parameters not discussed in Section 4.2.

4.3 Convolving the models

The final step before the model image can be compared to the observational data is to convolve it with a PSF, chosen from our PSF library generated by the observation of calibrator objects. The model image is rotated to the same position angle as the observational data, then convolved with each of the PSFs in the relevant PSF library, shifted on a sub-pixel scale to match the position of the target data, and then the best PSF for convolution is chosen for each model image. The best PSF is found for each of the rotated images by comparing with observational data and calculating the χ^2_{shot} for each of the models, and the best convolved model is the one with the lowest χ^2_{shot}.

The process of choosing the best convolved image is described by equation (2),

$$\chi^2_{\text{shot,i}} = \min_j \sum_k \frac{(D_{\text{i,k}} - (M \otimes P_\text{j})_\text{k})^2}{\sigma^2_\text{k}}. \tag{2}$$

The χ^2_{shot} for each data image D, of which there are i, is calculated by finding the minimum of χ^2_{shot} value over the set of PSFs P, of which there are j, over all of the pixels with the index k; where σ^2_k is the variance over those pixels, accounting for readout noise, target shot noise, and background shot noise. Note that we deliberately choose not to attempt to model speckles and AO phase noise as additional uncertainties, as it is in principle not a fundamental noise source in a well characterized and calibrated AO imager. We do, however, scale our final reported uncertainties appropriately, as described in Section 6.2.

The rotated model image is convolved with all of the PSFs, and the best of these is chosen to calculate the χ^2_{shot} for the data image D_i.

These best χ^2_{shot} values for each image are then summed to find the total χ^2_{shot} value, χ^2_{tot},

$$\chi^2_{\text{tot}} = \sum_i \chi^2_{\text{shot,i}}. \tag{3}$$

This process of choosing the single best calibrator can in principle underfit the data in a similar way that the locally optimized combination of images (LOCI) algorithm underestimates the brightness of detected companions (Soummer, Pueyo & Larkin 2012). We checked that this type of systematic was not severe by verifying that many different calibrator images were chosen for differing target images. Given how flat the squared visibility versus baseline curve of the calibrators are when calibrated against each other (see Figs 3 and 4), this systematic is limited to missing flux in our model at up to the few per cent level in the outer portion of the disc. A more robust algorithm would need to develop a significantly larger set of model PSFs (e.g. from a linear combination of calibrator images) and marginalize over all possible PSFs, as described in Ireland (2016).

4.4 Model parameter estimation via MC in MC

All of the aforementioned steps and the parameter estimation are completed using our MCinMC technique. MCinMC is the use of the Monte Carlo radiative transfer code RADMC3D in combination with the Markov Chain Monte Carlo (MCMC) code EMCEE (Foreman-Mackey et al. 2013). Given the nature of the large parameter space, and the risk that some of the parameters may be correlated, an MCMC approach was taken to ensure that the best-fitting parameters were the global minimum, rather than a local minimum. EMCEE is an affine-invariant ensemble sampler, meaning that it is not affected by covariances between parameters. EMCEE uses a number of walkers to explore a parameter space. In this work, the walkers are initialized from a group of points in the *N*-dimensional parameter space and the parameter space is explored. EMCEE can be easily made parallel on to different compute cores to make the computations more efficient.

Once the best χ^2_{shot} for each individual data image and its corresponding rotated, convolved model image is calculated, the χ^2_{shot} values are summed and used to calculate the log likelihood of the model;

$$\ln(\text{likelihood}) = \frac{-\chi^2_{\text{tot}}}{2T_{\text{MC}}}, \tag{4}$$

where the total χ^2_{shot} is that calculated in equation (3), and T_{MC} is the EMCEE temperature, set so that scaling the error bars by $\sqrt{T_{\text{MC}}}$ would give a reduced χ^2 of 1. We choose this approach rather than adding additional uncertainty estimates to our data variance, in order to show how much better the fits could be if PSF models were improved. EMCEE uses the log likelihood to find the best model for the data. The reduced χ^2_{shot} is calculated from this log likelihood, given by:

$$\chi^2 = \frac{-\ln(\text{likelihood}) \times 2 \times T_{\text{MC}}}{n_{\text{pixels}} \times n_{\text{images}}}, \tag{5}$$

where the number of pixels in the image n_{pixels}, and the number of images n_{images} normalize over the degrees of freedom, making this the reduced χ^2_{shot}. The number of pixels in the image (n_{pixels}), is actually the number used in the calculation, rather than the total

Table 5. General parameters for the synthetic data set.

Parameters that will remain set	
Parameter	Value
Star temperature	10000 K
Star mass	$2.0\,M_\odot$
Star radius	$2.0\,R_\odot$
Disc mass	$10^{-3}\,M_\odot$
r_{wall}	50 au
δ_{wall}	0.1
Dust type	5.6 nm CP dust
Distance to object	100 pc

number of pixels in the image. The number of images (n_{images}) is the number of target star images.

5 SYNTHETIC DATA SET

Our method was tested by generating a synthetic data set within MCinMC and then running a full parameter exploration on the synthetic data. The synthetic data set was generated by convolving a RADMC3D model, with parameters as listed in Table 5, and the values in the column labelled 'Target' in Table 6 with a sequence of calibrator (PSF) images from HD 167666. When this data set was tested a different sequence of calibrator images (HD 170768) were used for generating the convolved model for comparison with the data. It was found that the method could recover the parameters of the initial model to within five standard deviations for all parameters, with our approximate method of accounting for PSF fitting uncertainties as described in Section 6.2.

5.1 Testing the synthetic data set with MCinMC

A model with a disc asymmetry and companion was used to generate the synthetic data set and then this data set was tested in the MCinMC code. The data set was tested as a symmetric, asymmetric, and asymmetric with companion model. The results of

this exploration are shown in Table 6, with figures of the results in Fig. 8. The target parameters are those used to construct the data set, listed as Target in Table 6.

The symmetric model is the worst fit for the synthetic data, at a reduced χ^2_{shot} of 67.5. For the symmetric model only, the inner wall radius and the inclination are the same (within uncertainties) as those used to generate the data, however most were still within a few standard deviations of the true values. Since the data are asymmetric with a companion, it is not surprising that the symmetric model does not fit the data well. The χ^2_{shot} for the symmetric model is more than twice that of the asymmetric model.

Most parameters for the asymmetric model are closer to those used to generate the data than the symmetric results are, and those closest to the parameters used are the two depletion factors, the radius of the inner disc, the radius of the first wall, the inclination, and the asymmetry parameters. The asymmetric model χ^2_{shot} of 27.3 is a large improvement over the symmetric fit.

The companion model has an improved, but similar χ^2_{shot} to the asymmetric model. The resulting fits to the 8–13 parameters for the companion fit are mostly within three standard deviations of the data. When the model is convolved with the PSF to generate the synthetic data, the partly resolved companion gives a signal similar to a low-order aberration, and our simplified error model does not take this into account adequately. Note that in this case, the companion separation is dominated by the *x* position (causing the slight deviations in the companion offset and position angle), which agrees reasonably well with the input model.

The residual images for both the asymmetric and companion models have obviously lower residuals than the symmetric model. The symmetric model residual shows that there is an asymmetry in the data that is not being fit with this model. The asymmetric and companion model residuals mostly show the noise in the PSFs, although there is a slight difference between the two at the companion position, showing that the companion model fits a feature where the asymmetric model cannot. The small uncertainty on the brightness of the companion and its position indicate that there is a strong asymmetry in that part of the disc.

Table 6. Results for the synthetic companion data.

Parameter	Target	Synthetic companion data Symmetric model	Asymmetric model	Companion model
Dust-to-gas ratio	1×10^{-2}	$1.51 \pm 0.47 \times 10^{-2}$	$6.56 \pm 1.80 \times 10^{-3}$	$1.12 \pm 0.11 \times 10^{-2}$
δ_d	1×10^{-4}	$7.87 \pm 1.61 \times 10^{-5}$	$1.27 \pm 0.20 \times 10^{-4}$	$9.83 \pm 0.60 \times 10^{-5}$
δ_1	1×10^{-2}	$8.89 \pm 1.42 \times 10^{-3}$	$1.22 \pm 0.14 \times 10^{-2}$	$1.11 \pm 0.08 \times 10^{-2}$
r_d (au)	0.5	0.39 ± 0.07	0.64 ± 0.08	0.42 ± 0.03
r_d (mas)	5	3.9 ± 0.7	6.4 ± 0.8	4.2 ± 0.3
r_1 (au)	10.0	10.0 ± 0.1	10.2 ± 0.1	9.95 ± 0.10
r_1 (mas)	100	100 ± 1	102 ± 1	99.5 ± 1.0
r_2 (au)	25.0	23.9 ± 0.6	23.3 ± 0.4	23.6 ± 0.5
r_2 (mas)	250	239 ± 6	233 ± 4	236 ± 5
Inclination (°)	30.0	29.7 ± 1.2	31.9 ± 1.1	30.7 ± 1.2
Position angle (°)	50.0	54.1 ± 2.9	57.4 ± 2.2	56.4 ± 2.0
Star offset (mas)	1.3	–	1.6 ± 0.3	1.1 ± 0.1
Star position angle (°)	90.9	–	79 ± 15	75 ± 13
Companion offset (mas)	180	–	–	186 ± 2
Companion position angle (°)	232.8	–	–	235.6 ± 2.2
Companion contrast (mag)	5.4	–	–	5.7 ± 0.2
Flux ratio	30.31	30.33	30.32	30.32
Reduced χ^2_{shot}	–	67.5	27.3	24.4
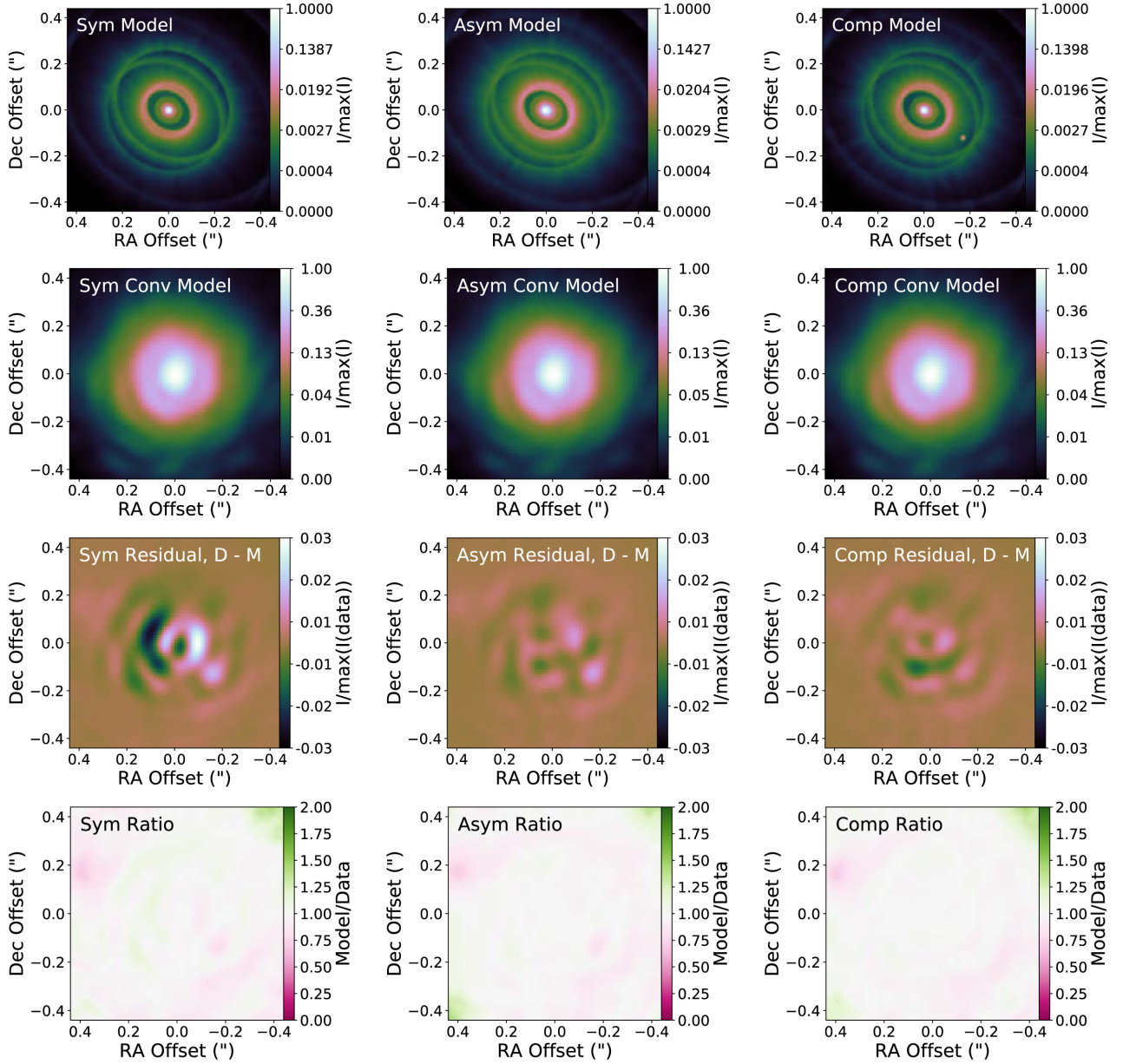
Figure 8. Converged results from the modelling of the synthetic companion data set. The left-hand column shows the symmetric model results, the middle shows the asymmetric model results, and the right-hand column shows the asymmetric with companion model results. The top row is the model image for each model type. The second row is the convolved model. The third row is the residual of the observed target data image minus the convolved model image. The fourth row is the ratio of the convolved model divided by the observed target data image.

5.2 Summary of synthetic data set results

In this test, our method is able to distinguish between a symmetric or asymmetric disc, but not as well between an asymmetry caused by an eccentric disc or a point-like asymmetry. The symmetric model will not fit well to a disc with obvious asymmetries. It is difficult to determine the cause of an asymmetry with our method, however we are sensitive to whether an asymmetry is present, and the strength of the asymmetry.

Our method is limited by the uncertainties in the PSFs, making it difficult to determine the difference between a disc asymmetry and a point-like asymmetry. Given the faint nature of planetary companions, it can be difficult to determine the difference between noise, disc asymmetries, and a point-like asymmetry.

6 RESULTS

6.1 Dust

It was initially found that carbon dust gave a better result (lower reduced χ^2_{shot}) than silicate dust; and that dust containing carbon and PAHs gave a better result than plain carbon dust. Carbon produced better models for Oph IRS 48 than silicate dust could, because silicates were too cool to produce the emission at ~10 au radii (Fig. 9). Relative to the absorption of stellar photons at $\lesssim 1\,\mu$m wavelengths, silicate dust has a large emission feature at 11 μm which effectively cools the dust (Draine 2003).

Using carbon dust, it was not possible to simultaneously have the ~13 au ring bright enough to fit our AO data and still have an inner

Midplane Temperature
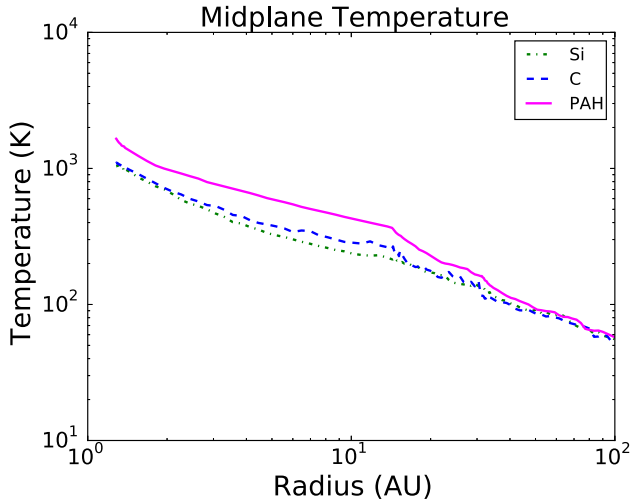
Figure 9. Temperature plots in the disc mid-plane for the different types of dust. Magenta solid line is CP dust, blue dashed line is carbon dust, and the green dotted–dashed line is silicate dust. The CP dust is warmer than the other dust types, particularly in the inner regions of the disc.

disc bright enough to fit the SED. The amount of carbon dust needed in the inner disc to fit the SED would cause too much shadowing on the 13 au ring. Therefore, a dust which could more effectively absorb blue and ultraviolet wavelengths was needed.

Both of the discs studied in this work have clear PAH features in their SEDs (e.g. Bruderer et al. 2014; Seok & Li 2016; Maaskant et al. 2014, Oph IRS 48, HD 169142, both, respectively). In our attempts to fit the near-IR excesses seen in the SED, CP dust was used, and the same dust was used for both objects due to the similarities in their SEDs. Given that we are not trying to fit the whole SED, we chose a dust model from the Draine & Li (2001, 2007) dust, which includes fine grained graphitic carbon, and PAHs. From inspection of the SEDs the dust chosen from the Draine & Li (2001, 2007) set of neutral CP dust has a grain size of 5.6 nm. Even though it is known that some of the PAHs in these discs are ionized (Maaskant et al. 2014), we chose the neutral dust to use in both cases because it was similar to the PAH emission of the objects and able to replicate the near-IR excess. For an investigation of how differently sized dust grains from the Draine & Li (2001, 2007) set of neutral CP dust change the fit to the SED, see the Appendix D.

The reason that the smaller grains (CP dust) better recover the near-IR excess is that they are generally warmer than larger grains (see Fig. 9), due to their relatively higher UV absorption. There is also no need to invoke quantum heating in this case, as ∼5 nm radius dust has a sufficient number of atoms to not be significantly warmed by single photon absorption events. Thus quantum heating in the disc is ignored here, though it may become required to model images at all wavelengths (especially even shorter wavelengths) simultaneously.

One consideration to be able to have both a bright inner disc and bright walls at 13 and 30 au (as is needed for Oph IRS 48, and similar to what is needed in HD 169142) would be to have in inclined inner disc. With an inclined inner disc, carbon dust could still be used and the disc walls would still be bright. However, for both Oph IRS 48 and HD 169142, the deconvolved images show symmetric features, with no evidence for the shadows that would be expected at opposite sides of the disc if the inner disc was inclined. Therefore, an inclined inner disc with carbon dust is not considered here and we instead use CP dust.

A mix of different dust types would benefit the modelling of the disc and the SED simultaneously. More freedom in the dust distribution and composition would allow for better modelling of disc features, and possibly determine the difference between a disc feature or a companion. This was not justified for our current method, given the high speckle residuals, which were at the same level for our data sets as for synthetic data sets using multiple calibrator stars.

6.2 Fits to Oph IRS 48 and HD 169142

The best-fitting model parameters for both objects are shown in Table 7. The primary fitting for HD 169142 was done for the 2014 data and for Oph IRS 48 it was done for the 2015 data, the fit for the best-fitting model for each of these data sets is then tested on the 2016 data. We do not report independent fits to the 2016 data because as mentioned in Section 2.2, some observations were taken through cloud.

In the following sections, the results of each model type for each object will be discussed. For each object there was a symmetric, an asymmetric, and a companion model tested. The model setups are described in Section 4.2. Figs 10 and 11 show each of these models; their convolved counterpart; the residual of the data and the model; and the ratio of the data and the model, for Oph IRS 48 and HD 169142, respectively, and are discussed in Sections 6.3 and 6.4.

The values and uncertainties quoted in Table 7 are the mean and standard deviation of the results found with EMCEE. The data used in this work have uncertainties with several components, including background and speckle noise.

We choose to only consider the target and background shot noise to give the reader a clear indication on the scope of improvement in model fitting that would be possible with an improved PSF model (e.g. interpolation between PSFs). However, we also need to robustly estimate statistical uncertainties from our current fitting method, and choose to do this by setting the temperature in the MCMC.

Naively, EMCEE temperature would be increased by the value of reduced $\chi^2_{\rm shot}$, which is equivalent to scaling error bars on the data pixels by $\sqrt{\chi^2_{\rm shot}}$ to give $\chi^2 = 1$ due to uncertainties in addition to the modelled shot noise. However, this does not take into account the highly correlated speckle noise, and would underestimate our final uncertainties. The speckle noise has a characteristic solid angle of correlated noise which is $\sim(\lambda/D)^2$, or $\sim N_{\rm ind} = 70$ pixels. Therefore, to account for the speckle noise we set the temperature in EMCEE ($T_{\rm MC}$) as $\sim N_{\rm ind} \times \chi^2_{\rm shot}$ ($\sim$10000), where $\chi^2_{\rm shot}$ is the reduced chi-squared of the best-fitting model. Thus, the $\chi^2_{\rm shot}$ of $\gg 1$ we have in our results means that photon statistics of the target and background do not dominate the uncertainty. We have not studied sufficient calibrator–calibrator pairs to redefine our uncertainties reliably (based on the noise from the speckles).

The main purpose of this work was to fit the inner regions of the disc, rather than the whole disc. The interested reader is directed to Appendix D for an investigation of the SEDs of the discs.

6.3 Oph IRS 48

For Oph IRS 48, the aim was to study the disc structure within ∼20 au and also to see if a companion could be detected. In our analysis of Oph IRS 48, the 2015 data were used, with the best model for each of the model types for the 2015 data tested on the 2016 data. Fig. 10 shows the resulting models, convolved images, residuals, and ratio images.

Table 7. Best-fitting model parameters for 2015 Oph IRS 48 data and 2014 HD 169142 data, using mean and standard deviation. Best-fitting models were not calculated for the 2016 data of both objects, however the best-fitting models from the other years were tested on the 2016 data.

Oph IRS 48

Parameter	Symmetric	Asymmetric	Companion
Dust-to-gas ratio	$3.10 \pm 0.66 \times 10^{-3}$	$3.20 \pm 0.26 \times 10^{-3}$	$2.06 \pm 0.09 \times 10^{-3}$
δ_d	$2.48 \pm 0.43 \times 10^{-4}$	$2.11 \pm 0.23 \times 10^{-4}$	$4.20 \pm 0.35 \times 10^{-4}$
δ_1	$1.01 \pm 0.10 \times 10^{-2}$	$9.40 \pm 0.61 \times 10^{-3}$	$1.24 \pm 0.06 \times 10^{-2}$
r_d (au)	1.6 ± 0.2	1.4 ± 0.1	2.0 ± 0.1
r_d (mas)	12 ± 1	10 ± 1	15 ± 1
r_1 (au)	15.0 ± 0.3	14.6 ± 0.1	15.2 ± 0.2
r_1 (mas)	112 ± 2	108 ± 1	113 ± 1
r_2 (au)	32.1 ± 0.9	31.0 ± 0.3	31.3 ± 0.3
r_2 (mas)	238 ± 7	231 ± 2	233 ± 2
Inclination (○)	54.8 ± 0.5	54.2 ± 0.3	52.4 ± 0.3
Position angle (○)	99.0 ± 0.6	98.8 ± 0.3	96.5 ± 0.4
Star offset (mas)	–	5.0 ± 0.4	5.3 ± 0.3
Star offset position angle (○)	–	118.7 ± 7.8	122.9 ± 8.2
Companion offset (mas)	–	–	104 ± 2
Companion position angle (○)	–	–	288.6 ± 4.6
Companion contrast (mag)	–	–	3.97 ± 0.05
Flux ratio (7.8)	7.8	7.8	7.8
Reduced χ^2_{shot}	65.1	60.0	48.0
Reduced χ^2_{shot} 2016 data	68.3	61.0	52.6

HD 169142

Parameter	Symmetric	Asymmetric	Companion[a]
Dust-to-gas ratio	$8.88 \pm 1.34 \times 10^{-4}$	$7.16 \pm 0.63 \times 10^{-4}$	$6.81 \pm 0.64 \times 10^{-4}$
δ_d	$6.14 \pm 0.57 \times 10^{-4}$	$7.14 \pm 0.47 \times 10^{-4}$	$7.17 \pm 0.42 \times 10^{-4}$
δ_1	$2.77 \pm 0.38 \times 10^{-2}$	$2.02 \pm 0.41 \times 10^{-2}$	$2.02 \pm 0.38 \times 10^{-2}$
r_d (au)	0.11 ± 0.01	0.11 ± 0.01	0.11 ± 0.01
r_d (mas)	0.96 ± 0.08	0.96 ± 0.08	0.96 ± 0.08
r_1 (au)	8.4 ± 0.4	7.3 ± 0.5	7.3 ± 0.4
r_1 (mas)	74 ± 4	64 ± 4	64 ± 4
r_2 (au)	15.4 ± 1.3	13.5 ± 0.6	13.4 ± 0.6
r_2 (mas)	135 ± 11	118 ± 5	118 ± 5
Inclination (○)	30.3 ± 1.0	29.8 ± 0.4	29.5 ± 0.6
Position angle (○)	12.6 ± 2.1	15.0 ± 0.9	15.7 ± 1.5
Star offset (mas)	–	0.09 ± 0.03	0.11 ± 0.03
Star offset position angle (○)	–	15.0 ± 9.1	7.4 ± 8.9
Companion offset (mas)	–	–	131 (fixed)
Companion position angle (○)	–	–	2.6 (fixed)
Companion contrast (mag)	–	–	5.7 ± 0.7
Flux ratio (5.2)	5.2	5.2	5.2
Reduced χ^2_{shot}	5.91	5.58	5.51
Reduced χ^2_{shot} 2016 data	44.1	42.8	45.7

Notes: [a]This model is not statistically significant. The additional parameters in this model are not justified by the data, but is included for completeness.

One commonality shared by the Oph IRS 48 models in their residual and ratio images in Fig. 10 is the two features (one on the left and one on the right of the disc) that are consistently present. These 'ear' features are green in the residuals and light green in the ratio images. They are present in the same location as where the model appears brighter at around 30 au ($\sim \pm 0.25$ arcsec), because of the overlap of the bright $\sim$30 au ring.

This region of the disc is expected to become optically thick with opacity dominated by large grains, but our model only includes very small grains as we focus on the inner regions. This issue with the 'ears' in the residual and ratio images could possibly be rectified by using a mixture of dust grains with varying sizes and compositions. There are some other features in the residual images that are consistent across all of the models, which may be due to an inadequate PSF library. As mentioned above when uncertainties were discussed, this noise is also the reason for the high reduced χ^2_{shot} values.

All three of the Oph IRS 48 models have similar values for the parameters. The symmetric and asymmetric models are most similar with nearly all parameters matching within uncertainties. The companion model is slightly different; as it must allow for the presence of the companion changing the brightness of the disc, thus adjusting the dust parameters and stellar position on accordingly. The similarities and differences between the models are discussed in the following sections.

6.3.1 Symmetric disc

The first column of Fig. 10 shows the results for the symmetric model. The residual and ratio images show how well the model fits the data. The L′ band flux ratio of 7.8 is a match for the value we were fitting to. The symmetric model of Oph IRS 48 has a bright inner disc, r_1 at $\sim$112 mas ($\sim$15 au) and r_2 at $\sim$238 mas ($\sim$32.1 au). The location of r_1 is consistent with the location of
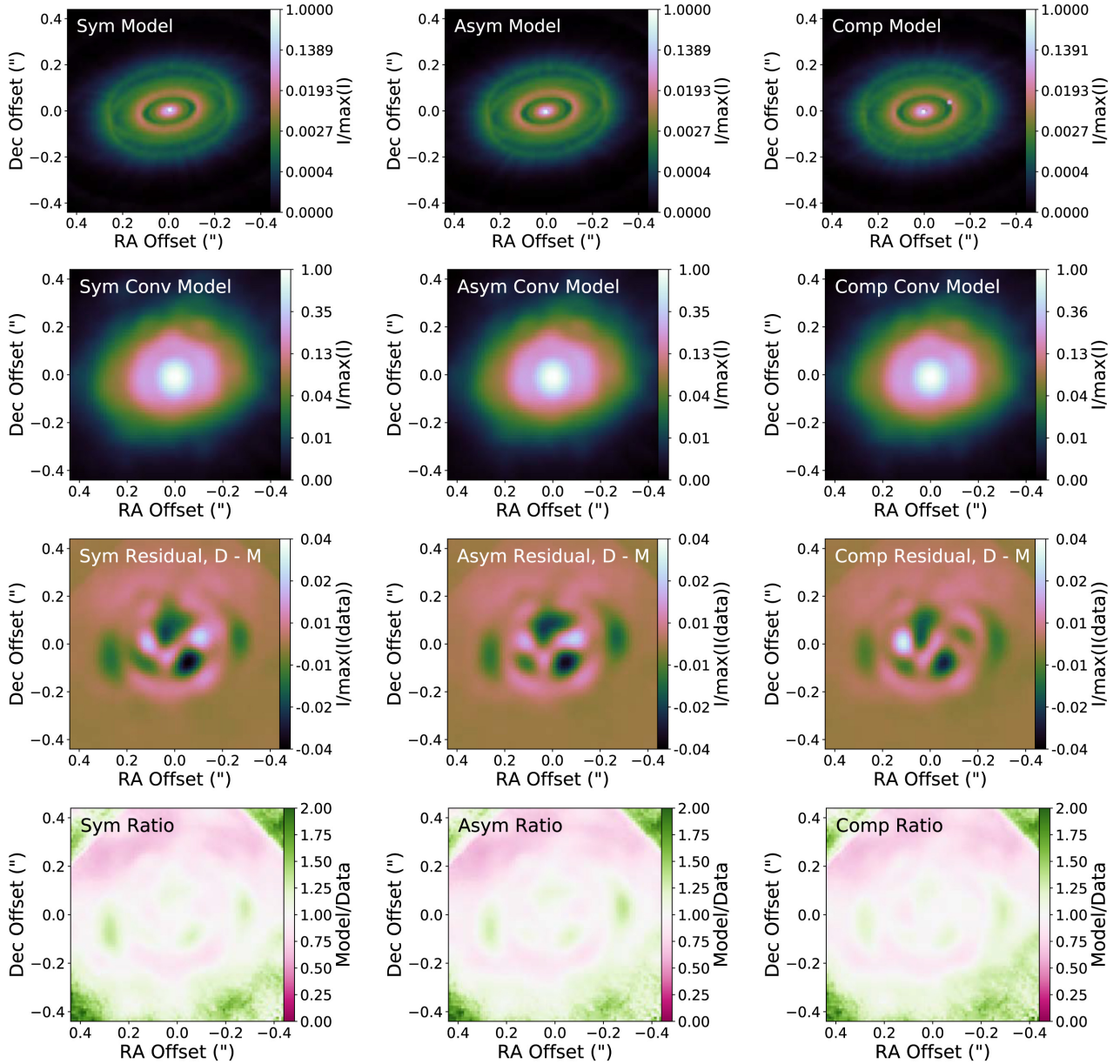
Figure 10. Converged results from the modelling of Oph IRS 48. The left-hand column shows the symmetric model results, the middle shows the asymmetric model results, and the right-hand column shows the companion model results. The top row is the model image for each model type. The second row is the convolved model. The middle row is the residual of the observed target data image minus the convolved model image. The fourth row is the ratio of the convolved model divided by the observed target data image. The bottom row is a plot of the mid-plane density profile of the disc.

the PAH emission modelled by Geers et al. (2007b, ∼16 au), and the rings suggested by Brown et al. (2012b, ∼15 and ∼34 au).

6.3.2 Asymmetric disc

As mentioned before, the asymmetry in the disc was introduced by moving the star. This introduces two new parameters that the symmetric model did not have, the star offset and position angle (generated from the *x* and *y* positions of the star). Because there are additional parameters a better fit is expected, and in this case a slightly better fit is achieved for the 2015 data.

Aside from the two new parameters, most of the parameter values are the same within uncertainties as for the symmetric model case.

6.3.3 Asymmetric disc with companion

As mentioned earlier, a companion is added to the asymmetric model by including a second RADMC3D point source. The results for the planet model differ slightly from the asymmetric and symmetric models for the parameters relating to the dust structure. This is because having the second source causes some changes to the brightness of the disc. The values of r_1 and r_2 are similar to those of the symmetric and asymmetric models, but r_d has moved slightly further out.

The companion has a brightness contrast of 3.97 ± 0.05 mag with respect to the rest of the image. Note that this is a factor of ∼30 fainter than the disc emission or a factor of ∼5 fainter than the local disc emission within a diffraction limit (∼80 mas). The position of our point-like asymmetry at ∼104 mas and ∼288° is
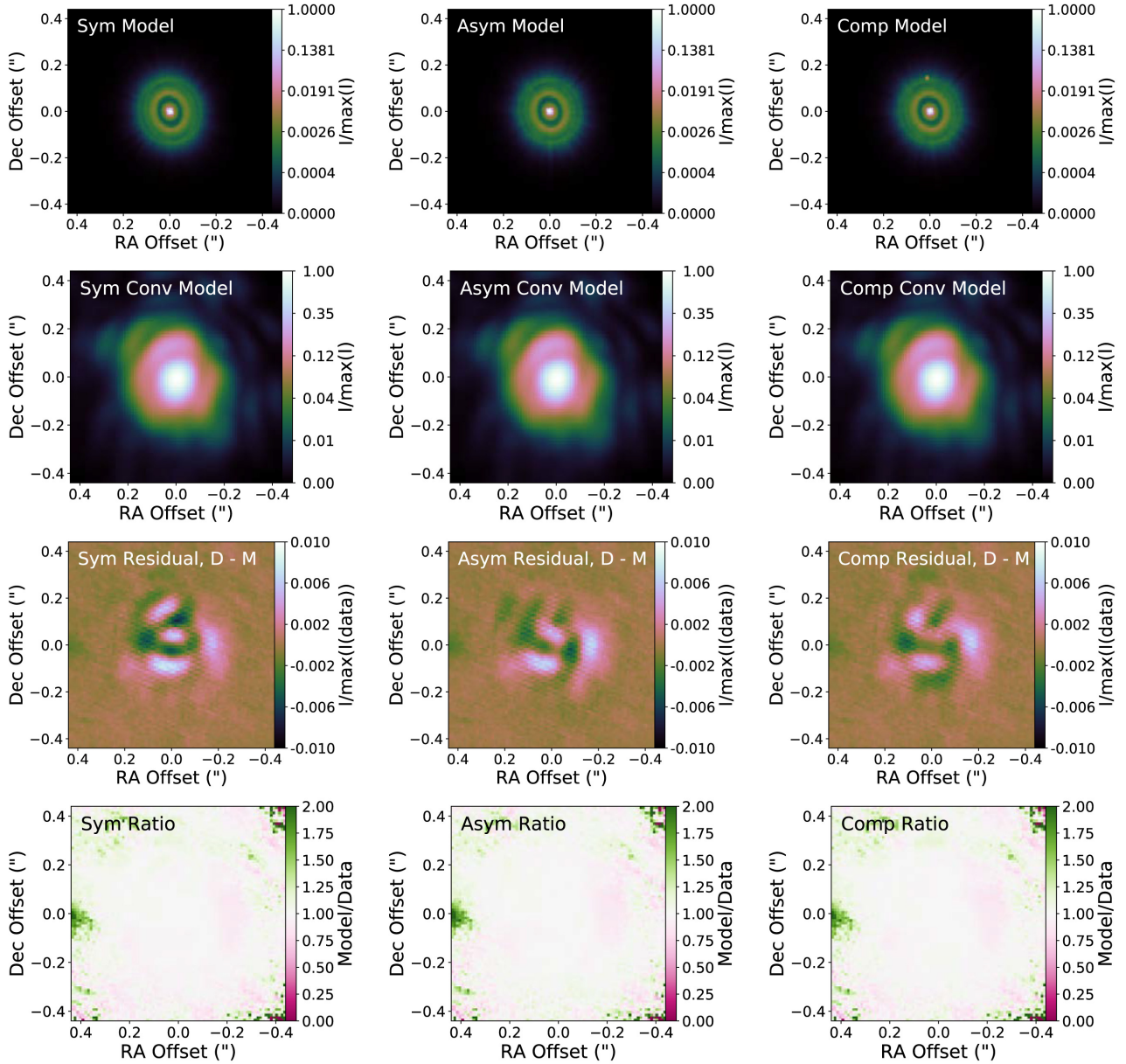
Figure 11. Results from the modelling of HD 169142. The layout is the same as for Fig. 10.

consistent with one of the point sources found by Schworer et al. (2017) at ∼105 mas to the west of the star. However, the Schworer et al. (2017) object has a contrast of ∼3.3 mag.

The reduced χ^2_{shot} for this more complex model is the lowest of the three models for both 2015 and 2016, as reported in Table 7.

6.3.4 Summary of Oph IRS 48 results

The disc parameters are similar across all models for Oph IRS 48, however there is improvement with the addition of an asymmetry and a companion. Given this improvement, the small uncertainty in the companion radius and the narrow brightness contrast range, it is likely that there is an asymmetry in this region of the Oph IRS 48 disc. However, we are unable to identify whether this is due to a disc asymmetry or a point-like companion at this stage.

In all cases, the inner disc radius (r_d) is greater than what is considered to be the canonical inner disc for Oph IRS 48. Schworer et al. (2017) find using imaging and SED fitting that there is likely

no emission from the disc between 0.4 and 1 au, and that the very small particles in the disc are present from 11 au. We find that for the disc to be bright enough to match our observations, we do still require the inner disc, but present beyond 1 au, with a second ring of emission present at ∼15 au (∼112 mas).

Generally for Oph IRS 48 the χ^2_{shot} values are quite high. Some part of this high χ^2_{shot} is likely not only due to an inadequate PSF library, but also due to insufficient complexity in the model, as evidenced by the negative residuals to the east and west at ∼0.25 arcsec separation.

6.4 HD 169142

One goal of the study on HD 169142 was to see if we could detect the candidate companion proposed to be in the inner disc. For HD 169142, the 2014 data were used for the analysis, with the best model for each of the model types for the 2014 data tested on the 2016 data. The results of each model type are discussed below,

and the figures corresponding to the model are shown in Fig. 11. The same model types and figures are included here as were in the previous Section 6.3 for Oph IRS 48.

The inclination and position angle in all cases for the HD 169142 disc are different to those in the literature. The inclination we find here is ∼30°, rather than the ∼13° reported in Panić et al. (2008), and our position angle is ∼15° compared to their ∼30°. This difference may arise from the large difference in the spatial scales probed: the Panić et al. (2008) observations using rotational lines of CO probed > 1 arcsec separations compared to our ∼0.1 arcsec separations. A disc warp, for example, could produce these slightly differing inner and outer disc geometries.

6.4.1 Symmetric disc

For the symmetric model, the best fit has r_1 at 74 mas (∼8.4 au), with r_2 at 135 mas (15.4 au). Previous studies of the disc found a ring at ∼175 mas (∼20 au), using modelling of the SED based on mid-IR observations (Honda et al. 2012) and imaging of large grains from 7mm observations (Osorio et al. 2014). Our deconvolved image of HD 169142 suggested a single ring at ∼88 mas (∼10 au), similar to that marginally detected by Ligi et al. (2018, ∼100 mas). We attempted modelling HD 169142 with one wall, but found that the $\chi^2_{\rm shot}$ values were significantly lower when we used two walls.

The reduced $\chi^2_{\rm shot}$ for the 2014 data was 5.91 and for the 2016 data, it was 44.1. There is more of a discrepancy between the results than there was for Oph IRS 48, likely due to the very significant difference in the observing conditions in this case (flux varying by a factor of ∼2 during observations even after removing the most cloud-affected data) and this χ^2 metric only taking shot noise into account (Section 4.3).

6.4.2 Asymmetric disc

The results for the asymmetric model are similar to the symmetric model. The results fit the symmetric ones within a few standard deviations. For this model r_1 is at 64 mas (∼7.3 au), with r_2 at 118 mas (∼13.5 au). The location of the star to generate the asymmetry is 3σ from the origin, suggesting that the star may not be off centre in HD 169142, in contrast to findings by Bertrang (2018). The reduced $\chi^2_{\rm shot}$ value for the asymmetric model is 5.58, which is a slight improvement over the symmetric model. The reduced $\chi^2_{\rm shot}$ of the 2016 data is 42.8 using the asymmetric model.

6.4.3 Asymmetric disc with companion

The companion model has a similar density structure to both the symmetric and asymmetric models. There is a wall at 64 mas (7.3 au), similar to the wall found in the symmetric and asymmetric models, as well as a wall at 118 mas (∼13.4 au). When the companion position was freely explored, it was not detected in any location with certainty. However, when the companion is placed at a location consistent with those found in the Biller et al. (2014) and Reggiani et al. (2014) studies (these are consistent with each other within the uncertainties), the $\chi^2_{\rm shot}$ was improved and the brightness contrast was found to be 5.7 ± 0.7 mag. Our companion is at a lower significance than those papers, and not as significant as a general disc asymmetry. Our brightness contrast is roughly consistent with the 6.5 ± 0.5 mag found by Reggiani et al. (2014), and the ∼6.4 mag reported by Biller et al. (2014). This point-like asymmetry is a factor of ∼100 fainter than the disc emission or a factor of ∼20 fainter than the local disc emission within a diffraction limit (∼80 mas).
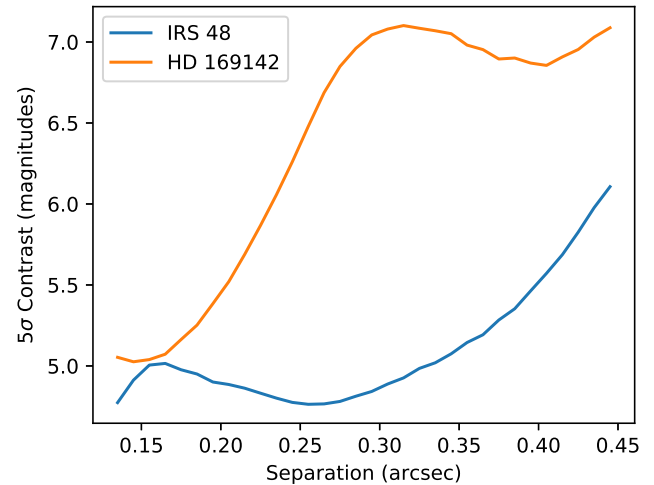
Figure 12. Detection limits as companion flux divided by total flux for additional companions fitted to the residuals of our disc models. These limits are not adequate to detect the majority of additional potential companions suggested in the literature.

For the 2016 data, the reduced $\chi^2_{\rm shot}$ is 45.7, which is slightly higher than for the asymmetric model.

6.4.4 Summary of HD 169142 results

In summary, the results of the HD 169142 models are consistent with each other, and indicate the presence of an asymmetry in the disc. We are able to recover the previously detected companion-like asymmetry, but are unable to determine the cause of the asymmetry at this stage. We also detect symmetric rings of dust at ∼61 mas (∼7 au) and ∼114 mas (∼13 au). Our rings are at a similar location to the ∼100 mas (∼11 au) ring and asymmetry found by Ligi et al. (2018). The location of our inner disc ($r_{\rm d}$) is at 0.11 au (0.96 mas), which is slightly beyond the radius of 0.07 au found by Chen et al. (2018) from their modelling of the inner disc.

The substantial difference between the $\chi^2_{\rm shot}$ values for the 2014 and 2016 epochs for HD 169142 is due to the large variation in observing conditions between epochs. As discussed in Section 2.2, the observing conditions for the 2016 epoch were affected by weather, particularly HD 169142.

6.5 Additional companions

We attempted to fit additional wide companions to our model residuals (i.e. companions present in addition to the companions fit in Sections 6.3.3 and 6.4.3), assessing the significance of companion fits by comparing fitted companion brightness to the rms azimuthally averaged contrast as a function of separation. No additional companions were detected, and the resulting contrast limits are shown in Fig. 12, with contrasts between 5 and 7 mag with respect to the system absolute L′ magnitudes of ∼ − 0.6 mag for Oph IRS 48 and ∼0.6 mag for HD 169142. The relatively poor contrast for Oph IRS 48 is likely due to the inadequacy of our model in fitting the disc structure, resulting in relatively high residuals. Additional companions would be detectable if they exist in the space below the lines in Fig. 12.

The possible 3.5 M_J object at 40 au (0.3 arcsec) discussed in Schwörer et al. (2017), deduced from disc structure and not from direct planetary emission, would then not be detectable in our data, unless it had a very high accretion rate of ∼3 × 10⁻⁵ M_J yr⁻¹

according to the models of Zhu (2015). Note that our companion model is consistent with the asymmetry seen by Schworer et al. (2017) which is interpreted as an asymmetric ring. Potential companions aside from those near the location of the Biller et al. (2014), Reggiani et al. (2014), and Ligi et al. (2018) candidates in HD 169142 include those suggested by Pérez et al. (2019), which is at beyond 0.5 arcsec; Gratton et al. (2019), at a distance of 0.335 arcsec, but a contrast of 10.1 mag; and Pohl et al. (2017), one of which is at our inner limit and the other beyond our limit; thus none of these would be detectable with this method.

7 CONCLUSIONS

Here, we introduced our method for the study of transitional discs. The method utilizes images of target and calibrator stars taken with a thermal IR filter behind AO to reveal detail about the structures of their discs. We use our new MCinMC (see Section 4) code to make models of the observed discs, then convolve the models with calibrator images, and finally compare the convolved models with the data to determine how well the model fits our data. The key conclusions we draw from this work are summarized here:

(i) In contrast to the historical view of transitional discs, we find that the 'gap' region in two Herbig Ae stars is radiatively dominated by emission from very small ($\lesssim 5$ nm) grains and PAHs. This has been suggested before for both objects, and this paper confirms their presence with spatially resolved detections.

(ii) We confirm previously reported brightness asymmetries (Biller et al. 2014; Reggiani et al. 2014; Schworer et al. 2017) in both HD 169142 and Oph IRS 48 using our complementary technique. However, the detection of overall disc asymmetry (modelled as an offset central star) was more significant than a point source companion model. For both objects, the colocated disc emission (within a diffraction limit) was brighter than previously reported 'companions' by a factor of ~5 or more, leading us to conclude that there is no need to invoke companions as anything more than a modelling convenience to explain the asymmetric emission.

The structure we detect in these discs suggests that the most common explanation of transitional discs having cleared inner holes may be too simple. To better understand these transitional discs and the mechanisms within them, we need more complete models of the disc geometry and composition and an improved understanding of the PSF uncertainties in the observational data.

An improvement that could be made to our method would be to interpolate between the PSFs and to use a larger library, possibly incorporating multiple nights of observations or models of optical aberrations, in a similar way to LOCI (Lafrenière et al. 2007) or KL eigenimages (Soummer et al. 2012). These methods will ultimately be limited by the angular resolution of a single telescope, and improved spatial resolution with the Multi AperTure mid-Infrared SpectroScopic Experiment (MATISSE, Lopez et al. 2014) or future concepts such as the Planet Formation Imager (Ireland et al. 2016) may be required to definitively distinguish between disc features and signs of exoplanets.

REFERENCES

Barbary K., 2016, Extinction v0.3.0,

Bertrang G. H.-M., Avenhaus H., Casassus S., Montesinos M., Kirchschlager F., Perez S., Cieza L., Wolf S., 2018, MNRAS, 474, 5105

Biller B. A. et al., 2014, ApJ, 792, L22

Brown J. M., Herczeg G. J., Pontoppidan K. M., van Dishoeck E. F., 2012a, ApJ, 744, 116

Brown J. M., Rosenfeld K. A., Andrews S. M., Wilner D. J., van Dishoeck E. F., 2012b, ApJ, 758, L30

Bruderer S., van der Marel N., van Dishoeck E. F., van Kempen T. A., 2014, A&A, 562, A26

Cardelli J. A., Clayton G. C., Mathis J. S., 1989, ApJ, 345, 245

Castelli F., Kurucz R. L., 2004, in Piskunov N., Weiss W. W., Gray D. F., eds, Proc. IAU Symp., Modelling of Stellar Atmospheres, Poster Contributions. Astron. Soc. Pac., San Francisco, p. A20

Chen L., Kóspál Á., Ábrahám P., Kreplin A., Matter A., Weigelt G., 2018, A&A, 609, A45

Cutri R. M. et al., 2003, 2MASS All Sky Catalog of point sources., The IRSA 2MASS All-Sky Point Source Catalog

Dodson-Robinson S. E., Salyk C., 2011, ApJ, 738, 131

Draine B. T., 2003, ARA&A, 41, 241

Draine B. T., Li A., 2001, ApJ, 551, 807

Draine B. T., Li A., 2007, ApJ, 657, 810

Dullemond C. P., 2012, Astrophysics Source Code Library, record ascl: 1202.015

Elias J. H., 1978, ApJ, 224, 453

Erickson K. L., Wilking B. A., Meyer M. R., Robinson J. G., Stephenson L. N., 2011, AJ, 142, 140

Fedele D. et al., 2013, A&A, 559, A77

Fedele D. et al., 2017, A&A, 600, A72

Foreman-Mackey D., Hogg D. W., Lang D., Goodman J., 2013, PASP, 125, 306

Gaia Collaboration et al., 2018, A&A, 616, A1

Geers V. C., Pontoppidan K. M., van Dishoeck E. F., Dullemond C. P., Augereau J.-C., Merín B., Oliveira I., Pel J. W., 2007a, A&A, 469, L35

Geers V. C., van Dishoeck E. F., Visser R., Pontoppidan K. M., Augereau J.-C., Habart E., Lagrange A. M., 2007b, A&A, 476, 279

Gratton R. et al., 2019, A&A, 623, A140

Han E., Wang S. X., Wright J. T., Feng Y. K., Zhao M., Fakhouri O., Brown J. I., Hancock C., 2014, PASP, 126, 827

Helou G., Walker D. W., 1988, in Infrared Astronomical Satellite (IRAS) Catalogs and Atlases: The Small Structure Catalog, Vol. 7, p. 1

Honda M. et al., 2012, ApJ, 752, 143

Ireland M. J., 2013, MNRAS, 433, 1718

Ireland M. J., 2016, in Boffin H. M. J., Hussain G., Berger J.-P., Schmidtobreick L., eds, Astrophysics and Space Science Library Vol. 439, Astronomy at High Angular Resolution, Springer International Publishing, Switzerland. p. 43

Ireland M. J. et al., 2016, Proc. SPIE, Vol. 9907, Status of the Planet Formation Imager (PFI) concept, SPIE, Bellingham, p. 99071L

Ishihara D. et al., 2010, A&A, 514, A1

Jayawardhana R., Fisher R. S., Telesco C. M., Pi na R. K., Barrado y Navascués J., Hartmann L. W., Fazio G. G., 2001, AJ, 122, 2047

Kanagawa K. D., Muto T., Tanaka H., Tanigawa T., Takeuchi T., Tsukagoshi T., Momose M., 2015, ApJ, 806, L15

Kraus S. et al., 2013, ApJ, 768, 80

Labeyrie A., 1970, A&A, 6, 85

Lada C. J., 1987, Star Formation - From OB associations to protostars, Star Forming Regions, 115, 1

Lafrenière D., Marois C., Doyon R., Nadeau D., Artigau É., 2007, ApJ, 660, 770

Ligi R. et al., 2018, MNRAS, 473, 1774

Loinard L., Torres R. M., Mioduszewski A. J., Rodríguez L. F., 2008, ApJ, 675, L29

Lopez B. et al., 2014, The Messenger, 157, 5

Lucy L. B., 1974, AJ, 79, 745

Maaskant K. M., Min M., Waters L. B. F. M., Tielens A. G. G. M., 2014, A&A, 563, A78

Maaskant K. M. et al., 2013, A&A, 555, A64

Macías E., Anglada G., Osorio M., Torrelles J. M., Carrasco-González C., Gómez J. F., Rodríguez L. F., Sierra A., 2017, ApJ, 838, 97

Mari nas N., Telesco C. M., Fisher R. S., Packham C., 2011, ApJ, 737, 57

Marsh K. A., Mahoney M. J., 1992, ApJ, 395, L115

Marsh K. A., Mahoney M. J., 1993, ApJ, 405, L71

McClure M. K. et al., 2010, ApJS, 188, 75

Meeus G. et al., 2010, A&A, 518, L124

Monnier J. D. et al., 2017, ApJ, 838, 20

Osorio M. et al., 2014, ApJ, 791, L36

Panić O., Hogerheijde M. R., Wilner D., Qi C., 2008, A&A, 491, 219

Pohl A. et al., 2017, ApJ, 850, 52

Pérez S., Casassus S., Baruteau C., Dong R., Hales A., Cieza L., 2019, preprint (arXiv:1902.05143)

Quanz S. P., Avenhaus H., Buenzli E., Garufi A., Schmid H. M., Wolf S., 2013, ApJ, 766, L2

Reggiani M. et al., 2014, ApJ, 792, L23

Richardson W. H., 1972, J. Opt. Soc. Am. (1917-1983), 62, 55

Salyk C., Herczeg G. J., Brown J. M., Blake G. A., Pontoppidan K. M., van Dishoeck E. F., 2013, ApJ, 769, 21

Schwörer G. et al., 2017, ApJ, 842, 77

Seok J. Y., Li A., 2016, ApJ, 818, 2

Seok J. Y., Li A., 2017, ApJ, 835, 291

Skrutskie M. F., Dutkevitch D., Strom S. E., Edwards S., Strom K. M., Shure M. A., 1990, AJ, 99, 1187

Soummer R., Pueyo L., Larkin J., 2012, ApJ, 755, L28

Strom K. M., Strom S. E., Edwards S., Cabrit S., Skrutskie M. F., 1989, AJ, 97, 1451

Sylvester R. J., Skinner C. J., Barlow M. J., Mannings V., 1996, MNRAS, 279, 915

Thalmann C. et al., 2010, ApJ, 718, L87

van der Marel N., Pinilla P., Tobin J., van Kempen T., Andrews S., Ricci L., Birnstiel T., 2015, ApJ, 810, L7

van der Marel N. et al., 2013, Science, 340, 1199

van Kempen T. A., van Dishoeck E. F., Salter D. M., Hogerheijde M. R., Jørgensen J. K., Boogert A. C. A., 2009, A&A, 498, 167

Walker H. J., Wolstencroft R. D., 1988, PASP, 100, 1509

Wilking B. A., Lada C. J., Young E. T., 1989, ApJ, 340, 823

Wright E. L. et al., 2010, AJ, 140, 1868

Yamamura I., Makiuti S., Ikeda N., Fukuda Y., Oyabu S., Koga T., White G. J., 2010, AKARI-FIS Bright Source Catalog Release Note, Version 1, http://www.ir.iras.jaxa.jp/AKARI/Observation/PSC/Public/RN/AKARI-FIS_BSC_V1_RN.pdf

Zacharias N., Monet D. G., Levine S. E., Urban S. E., Gaume R., Wycoff G. L., 2004, The Naval Observatory Merged Astrometric Dataset, American Astronomical Society Meeting Abstracts, Vol. 205, #48.15

Zhu Z., 2015, ApJ, 799, 16

APPENDIX A: PARAMETER CONVERGENCE STUDY

A convergence test was completed to determine the optimal number of photon packets to use in the model, so that it was stable, but not too computationally expensive. It was found that 10^6 photon packets was good choice for the RADMC3D thermal Monte Carlo to converge. As seen in the plot in Fig. A1, there is a minimum for reduced χ^2_{shot} for the best model found with 10^4 or 10^5 photon packets, because increasing the number of photon packets changed the best-fitting parameters.

The convergence test used half and double the number of points in each parameter for the number of grid points. The result was that these different grids give a very similar χ^2_{shot} values to the one shown in Table A1.
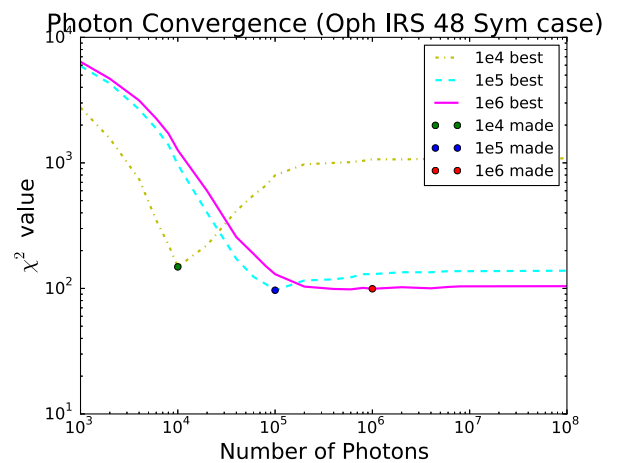
Figure A1. Convergence plots for different numbers of photons. The yellow dotted–dashed line is the model that was found to be the best using 10^4 photons, tested at different numbers of photons. The cyan dashed line is the model that was found using 10^5 photons, tested at different numbers of photons. The solid magenta line was found using 10^6 photons, and is the one chosen to be used in the modelling. The dots show where each different model for the numbers was found to have the best χ^2_{shot}.

Table A1. Values used for the spatial grid in RADMC3D.

Variable	Grid limits	Number of points between grid limits
r (au)	$r_{dust}, r_1, r_1 + 0.1, r_2, r_2 \times 1.1, 100$	5, 20, 30, 20, 40
θ	$0, \pi/3., \pi/2., 2\pi/3., \pi$	10, 30, 30, 10
ϕ	$0, 2\pi$	60

APPENDIX B: PARAMETERS FOR THE COMPANION BRIGHTNESS

In all cases, the companion had a temperature of 3500 K and a mass of 10^{-3} M$_\odot$, these were chosen due to modelling constraints. The brightness of the companion was adjusted by changing its radius, with a larger radius making the companion brighter. There was a lower limit on the radius of the companion, 0.02 R$_\odot$, which had a negligible amount of flux, and we found that this was not important to the determination of the log likelihood.

APPENDIX C: ADDITIONAL RADMC3D PARAMETERS

Geometric parameters for the spatial grid are shown in Table A1, and additional parameters that were used (many of which did not deviate from the defaul RADMC3D values) are shown in Table C1.

## APPENDIX D: SPECTRAL ENERGY DISTRIBUTIONS AND DUST TYPES

The SED of the symmetric disc model for Oph IRS 48 (left) and HD 169142 (right) are shown in Fig. D1. The SED models are reddened to match the photometry of each of the objects, and are included to show that without explicitly trying to fit the SED we are able to replicate the shape. The references for the data used in the SEDs can be found in Table D1.

For Oph IRS 48, it is difficult to deredden the photometry or redden the model, because there is so much extinction towards it. We use the Cardelli, Clayton & Mathis (1989) reddening laws with $R_V = 6.5$ and $A_V = 12.9$, as was found in Schwörer et al. (2017). To calculate the level of reddening that was to be applied we used the EXTINCTION package for PYTHON by Barbary (2016).

We note that the SED is not fit very well by our model, and this is due to the constraints we have placed on ourselves for modelling the

Table C1. Set parameters for all models, most are defaults that RADMC3D chooses, from the 'problem_params.inp' file.

Parameter	Value
Continuous stellar source	False
Discrete stellar source	True
Coordinate system	Spherical
Number of points for wavelength grid	19, 50, 30
Number of points for wavelength grid (SED)	100, 100, 30
Bounds of wavelength grid (μm)	0.1, 7.0, 25.0, 10000
Bounds of wavelength grid (μm) (SED)	0.1, 1.5, 25.0, 10000
Number of refinement levels	3
Number of the original grid cells to refine	3
Number of grid cells to create in a refinement level	3
Bulk density of materials (gcm^{-3})	3.6, 1.8
Grain size distribution power exponent	-3.5
Maximum grain size	10.0
Minimum grain size	0.1
Mass fractions of the dust components to be mixed	0.75, 0.25
Number of grain sizes	1
Use finite size of star	No – take as point source
Modified random walk	Off
Number of photons for image generation	2×10^4
Number of photons for SED generation	1×10^5
Output format for RADMC3D files	ASCII
Scattering mode	Isotropic
Dust temperature equal gas temperature	Yes
Background density (g cm^{-3})	1×10^{-30}
Pressure scale height at innermost radius (au)	0.0
Reference radius at which H_p/R is taken (au)	100.
Ratio of the pressure scale height over radius at reference radius for H_p/R	0.1
Flaring index	1./7.
Power exponent of the surface density distribution as a function of radius	-1.0
Outer boundary of the puffed-up inner rim in terms of innermost radius	0.0
Outer radius of the disc AU	100.
Surface density at outer radius of the disc	0.0
Surface density type	polynomial
Outer boundary of the smoothing in the inner rim in terms of innermost radius	1.0
Power exponent of the density reduction inside of the inner rim smoothing	0.0
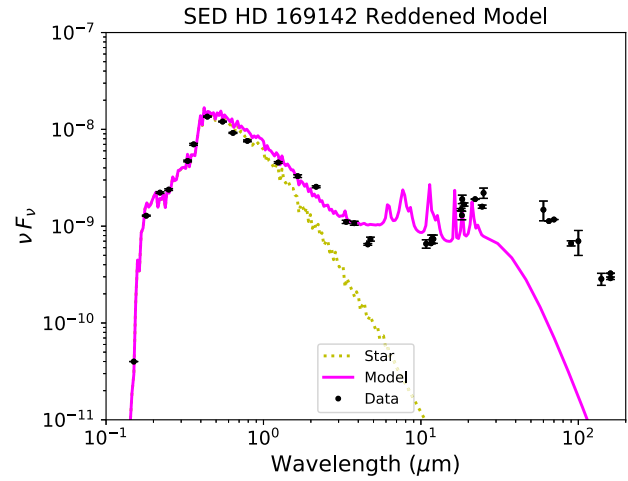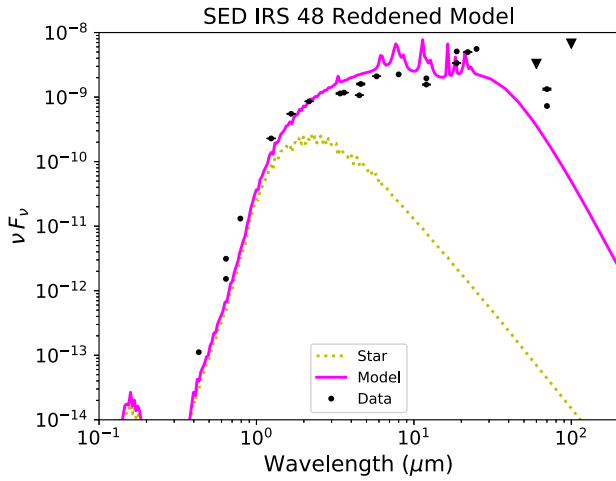
Figure D1. Shown here are the SEDs for the symmetric models in Table 7. Left is Oph IRS 48 with the photometry data and a reddened model, and right is HD 169142 with the photometry data and a reddened model. The model does not fit all of the data points at all wavelengths (especially not in the unmodelled outer disc), but it does replicate the general shape of the observed SED. The black dots are the photometric data taken from literature, and the black triangles represent upper limits, see Table D1 for the references associated with these data.

Table D1. References for SED data for Oph IRS 48 and HD 169142.

Oph IRS 48	
Wavelength (μm)	Reference
0.43, 0.64	Zacharias et al. (2004)
0.64, 0.79	Erickson et al. (2011)
1.24, 1.66, 2.16	Cutri et al. (2003)
3.4, 4.6, 12, 22	Wright et al. (2010)
3.6, 4.5, 5.8, 8, 70	van Kempen et al. (2009)
12, 25, 60 ,100	Helou & Walker (1988)
18.7	Yamamura et al. (2010)
18.7	Geers et al. (2007a)
70	Fedele et al. (2013)
HD 169142	
Wavelength (μm)	Reference
0.15, 0.18, 0.22, 0.25, 0.33	*IUE* archival data
0.36, 0.44, 0.55, 0.64, 0.79, 3.77, 4.78	Sylvester et al. (1996)
1.24, 1.65, 2.16	Two Micron All-sky Survey All-sky Point Source Catalog
3.35, 4.6, 11.6, 22.1	Wide-field Infrared Survey Explorer All-sky Data Release Catalog
10.8, 18,2	Jayawardhana et al. (2001)
11.7, 18.3	Mari nas et al. (2011)
12, 25, 60, 100	IRAS Point Source Catalog
18	AKARI/Infrared Camera All-sky Survey Point Source Catalog (Ishihara et al. 2010)
18.8, 24.5	Honda et al. (2012)
65, 90, 140, 160	AKARI/Far Infrared Surveyor All-sky Survey Point Source Catalog (Version 1.0)
70, 160	Meeus et al. (2010)
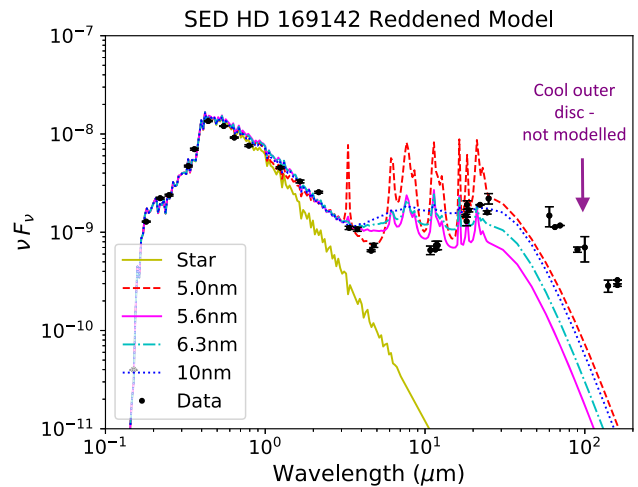
Figure D2. Shown here are the SEDs for the symmetric disc model of HD 169142 with different dust types. The solid yellow line is the model of the stellar photosphere. The dashed red line is for dust that has a 5.0 nm grain size, the solid pink line for dust that has 5.6 nm grains, the dotted–dashed cyan line is for dust with a grain size of 6.3 nm and the dotted blue line is for dust that is 10.0 nm. The purple arrow indicates the cool outer disc, which we are not attempting to fit here.

disc, as well as the large amount of extinction towards Oph IRS 48. A better fit could be achieved by differing dust types with radius, or with a different model configuration. As fitting the SED was not the key goal of this work, but fitting the Keck L′ filter data was, we leave detailed fitting of the SED for future work.

The SED of the symmetric model for HD 169142 (right of Fig. D1) is able to recover the flux at our target wavelength, but does not do well beyond this, particularly not in the un-modelled cool outer disc region. The model was reddened using the same methods as for Oph IRS 48, but with $R_V = 3.1$ and $A_V = 0.31$. A better fit could be achieved with a different model configuration, specifically one that allows for varying the dust chemistry and distribution of the disc.

We also tested HD 169142 with a few different dust sizes to investigate how grain size changed the fit to the SED. The results of these tests are found in Fig. D2. Each dust type was started from the best fit with the 5.6 nm dust and then the MCinMC code was run to find a best-fitting model for the new dust type. The grain sizes investigated were 5.0 , 6.3 , and 10.0 nm, with the 5.6 nm dust to compare to. The composition of the dust is all the same carbon and PAH dust mix as discussed above from the Draine & Li (2001, 2007) set of neutral carbon and PAH dust.

Dust smaller than the one used for our analysis has very strong emission from PAHs, whereas dust of a larger grain size has weaker PAH emission. Larger dust is too cool to recover the features we would like to replicate. The chosen dust size of 5.6 nm allows us

to have PAH features with some smoothing due to graphite. Using a significantly smaller dust would move into the realm of needing quantum heating of the dust particles, which would be difficult to parametrize for our model, so we chose to use dust models readily available from the literature.

This paper has been typeset from a TEX/LATEX file prepared by the author.